Cavitation erosion risk assessment for a marine propeller behind a Ro-Ro container vessel

Melissaris, Themistoklis; Schenke, Sören; Van Terwisga, Tom J.C.

DOI
10.1063/5.0131914

Publication date
2023

Document Version
Final published version

Published in
Physics of Fluids

Physics of Fluids

Cavitation erosion risk assessment for a marine propeller behind a Ro–Ro container vessel

Cite as: Phys. Fluids **35**, 013342 (2023); https://doi.org/10.1063/5.0131914
Submitted: 25 October 2022 • Accepted: 02 January 2023 • Accepted Manuscript Online: 03 January 2023 • Published Online: 30 January 2023

Themistoklis Melissaris, Sören Schenke and Tom J. C. van Terwisga

Physics of Fluids ARTICLE scitation.org/journal/phf

Cavitation erosion risk assessment for a marine propeller behind a Ro–Ro container vessel

Cite as: Phys. Fluids **35**, 013342 (2023); doi: 10.1063/5.0131914
Submitted: 25 October 2022 · Accepted: 2 January 2023 ·
Published Online: 30 January 2023

View Online Export Citation CrossMark

Themistoklis Melissaris,[1,2,a] Sören Schenke,[3] and Tom J. C. van Terwisga[1,4]

AFFILIATIONS

[1]Delft University of Technology, the Netherlands
[2]Propulsion Technology Department, Wärtsilä Netherlands BV, Drunen, Netherlands
[3]Otto-von-Guericke University Magdeburg, Germany
[4]Maritime Research Institute Netherlands, the Netherlands

Note: This paper is part of the special topic, Cavitation.
[a)]**Author to whom correspondence should be addressed:** themis.melissaris@wartsila.com

ABSTRACT

A novel cavitation erosion risk model, developed by Schenke *et al.* ["On the relevance of kinematics for cavitation implosion loads," Phys. Fluids **31**, 052102 (2019)], is applied to compute the cavitation implosion loads. The instantaneous energy balance during the collapse of cavitating structures is considered, where the initial potential energy is first converted into collapse-induced kinetic energy, before it is radiated to the surrounding surface at the final stage of the collapse. In this study, we focus on assessing the cavitation development and the risk of erosion on the blades of propellers operating behind a Ro–Ro container vessel. The presence of the hull contributes to the non-uniformity of the inflow. The consequent variation in velocities and angles of attack leads to the amplification of the cavitation dynamics, especially when the blade passes through the top position. Two designs are investigated that experience cavitation erosion on the pressure side. A statistical filter is used to attenuate low-amplitude implosion loads and identify the extreme events on the blade. The results show a very good correlation with the position of the actual erosion damage on the real propeller blades.

I. INTRODUCTION

The continuous restrictions on propeller noise and overall emissions, together with the increase in oil prices, enhance the need for maximum efficiency and optimum designs. As cavitation and cavita tion erosion is one of the major constraints in propeller design, one of the key factors to achieve optimum designs is to understand, predict, and resolve cavitation dynamics and cavitation nuisance. When the propeller is operating in behind condition, propeller cavitation and dynamics depend strongly on the inflow coming from the hull. Köksal *et al.*[1] showed that flow non-uniformity is one of the most dominant factors in cavitation and cavitation erosion intensity, compared to other factors, for instance, the cavitation number. That said, a good representation of the wakefield and the inflow toward the propeller seems very crucial for cavitating flow and erosion risk predictions.

Cavitation and its erosive potential is being investigated for over a century.[2] It was already known by Plesset and Prosperetti[3] that high-pressure peaks originating from the implosion of cavitation bubbles can be responsible for the damage on propeller blades. Isselin *et al.*[4] and Philipp and Lauterborn[5] showed that cavitation erosion is caused mainly by the collective collapse of bubbles in the vicinity of the solid boundary. Knapp[6] and Robinson and Hammitt[7] investigated the pitting rate by collapsing bubbles; however, the magnitudes of the implosion loads needed to form a pit were unclear. One of the first experimental attempts to identify the magnitude of the implosion loads from collapsing bubbles was done by Okada *et al.*,[8] and later on by Momma and Lichtarowicz.[9] Nevertheless, it still remained obscure whether erosion is caused by the collapse of individual bubbles close to the wall (liquid jet) or it is a result of the shock wave formation during a collapse of a bubble or a cloud. Plesset and Chapman[10] highlighted the potential of the liquid jet to cause erosion damage. Dular *et al.*[11] developed an erosion model based on this approach, showing that the impact of a micro-jet is the most profound mechanism from an implosion of a bubble in the vicinity of the wall. On the other hand, Fortes-Patella and Reboud[12] reached the conclusion that pressure waves emitted from cloudy structures as well as by micro-jet formation may be responsible for the damage. Joshi *et al.*[13] confirmed that the conclusion shows that even though the water hammer pressure can produce twice the maximum plastic deformation compared to a shock wave, the impacted volume is very small. On the other hand, the produced shock wave from a bubble collapse can plastify 800 times larger volume, leading to a higher erosion rate.

In addition to the micro-scale dynamics of micro-bubbles, the assessment of cavitation erosion on marine propellers requires analysis of the large-scale hydrodynamic mechanisms. One of the first attempts to investigate those mechanisms on marine propellers is described in the EROCAV observation handbook,[14] where the main principles of erosion assessment were based on cavitation kinematics and statistics. The proposed guidelines were extended by more detailed analysis of experimental observations,[15] and further supplemented by Bark and Bensow,[16] where detailed analysis principles are presented to better understand the mechanisms of cavitation erosion. Although these guidelines were written primarily for the analysis of experimental model or full-scale data, they proved to be essential for the development of numerical models for the assessment of propeller erosion.

Further experimental research on model scale[17–19] has shown that for full-scale predictions, numerical models can provide additional information for the erosive potential. Studies performed during the EROCAV project indicated that there is a clear need for improved methods for cavitation erosion prediction, and even though it was stated that experiments are and will be the only reasonable way to make such predictions,[20] assessment of cavitation erosion using CFD is becoming more popular recently. The first attempt to estimate the erosion risk numerically on marine propellers was focused on model scale. Hasuike *et al.*[21] used the erosion indices proposed by Nohmi *et al.*,[22] to investigate the risk of cavitation erosion in four differently loaded propellers. However, those indices seem quite empirical and their derivation unclear. Lu *et al.*[23] used LES to simulate the flow around two highly skewed propellers. They demonstrated that with suitable grid resolution, it is possible to identify the main difference in flow features caused by modest design alterations, while capturing the main mechanisms that are important in cavitation development. Such simulations could supplement experimental observations for identifying the erosion potential of collapsing cavitating structures. Usta *et al.*[24] and Usta and Korkut[25] estimated the erosion aggressiveness on a marine propeller using different indicators, as found in the literature; however, all the indicators, which are based on the energy balance method,[12] are highly dependent on the threshold of the method. Peters *et al.*[26] further developed the erosion model by Dular *et al.*,[11] based on the liquid-jet mechanism. They estimated the erosion potential on the propeller surface based on a coefficient derived from the number of impacts and their intensities. Although the specific model correctly represents the implosion loads originated from the hammer pressure and the micro-jet impacts, it ignores the implosion loads from the generated shock waves from the collapse of cloudy structures, that in large-scale dynamics seem to play a primary role as already discussed.

On the other hand, the collapses of small-scale cavitating structures created due to secondary shedding seem to be also associated with a high erosion risk.[27] Therefore, an ideal erosion model should be first combined with a solver capable of resolving large-scale and small-scale dynamics, and furthermore able to simulate the implosion loads originated both from shock wave and micro-jet formation. Arabnejad *et al.*[28] have proposed a numerical method to assess cavitation erosion using incompressible LES that considers both mechanisms. Although their method is based on the energy balance approach, the energy responsible for cavitation erosion is derived from the kinetic energy of the surrounding liquid and not from the potential energy contained in the collapsing cavitating structures. Therefore, they avoid the uncertainty of the collapse driving pressure. The application of their model on a commercial water-jet pump showed very promising results, as they could identify the regions of high erosion risk at different conditions, while obtaining good correlation with model test. The only possible drawback of this model is that since some assumptions need to be introduced to estimate the kinetic energy, the energy conservation is harder to control.

On the full scale, research on numerical assessment of propeller erosion potential is very limited. The generated pressures forming at the final stage of the collapse at extremely small scales require very high resolution in both space and time, rendering such simulations computationally inefficient. On top of that, incompressible solvers that are commonly used for engineering purposes fail to predict the peak pressures produced during the final stage of the collapse. Erosion models based on the maximum pressure during a collapse[29–32] are thus not suitable for such solvers. Therefore, alternative models should be considered to estimate cavitation implosion loads. Ponkratov and Caldas[33] and Ponkratov[34] investigated propeller and rudder erosion on the full scale using several functions, which were not reported. Peters *et al.*[26] applied their erosion model, based on the liquid jet mechanism, also on full-scale propellers. Nevertheless, resolving all the small scales and the micro-jet formation close to the wall, in complex propeller flows, increases significantly the computational cost, and especially in the design phase, a compromise needs to be made. Thus, in this study, we mainly focus on the dynamics of larger scales that can be resolved with URANS. Applying the correct mesh and time step resolution, we aim for an accurate prediction of the implosion loads that originated from the collapse of those larger structures. The consideration of the erosive potential of cavitating structures from an energy balance point of view[35,36] allows the use of an erosion model that employs the potential energy contained within the larger cavitating structures, as basis for the analysis of the surface impacts.[12,37–39] Moreover, the observations that a visual analysis of cavitation could give more insight into the hydrodynamic process of the global development of erosive cavities[14,16] illustrated that an erosion model based on the kinematics of the collapsing cavities could work ideally with pressure-based incompressible solvers. The key factor for such a model is the energy conservation as well as the overall and the instantaneous energy balance during the collapse.

The presented erosion model is a fully energy-conservative model that accounts for the temporal and spatial energy focusing toward the collapse center. Previous studies have shown that this model is able to predict the cavitation implosion loads in a quantitative manner.[40–42] The main feature that distinguishes this model from other energy balance-based models is the instantaneous energy balance consideration. The potential energy, initially contained in collapsing cavitating structures, is first converted into kinetic energy, during the collapse process, before it is radiated to the domain at the final stage of the collapse, as shock wave energy. In the presented study, the erosion risk on the propeller blades of a Ro–Ro container vessel is assessed. The erosion model is applied in the exact form as in one of our previous studies on a full-scale propeller;[42] however, this time the non-uniform

TABLE I. Main particulars of the ship.

Length between perpendiculars	165.0 m
Length overall	181.9 m
Length at waterline	173.3 m
Beam	28.8 m
Draught	9.99 m
Draught at aft PP	8.50 m
MCR	15 630 kW
Engine rate of revs	517 RPM
Design ship speed	19 knots

TABLE II. Main particulars of the propellers.

	Design 1	Design 2
Diameter	5.6 m	5.6 m
Number of blades	4	4
Expanded blade area ratio	0.638	0.665
Pitch diameter ratio (0.7R)	0.897	0.890
Hub diameter ratio	0.340	0.340
Direction of rotation	Left handed	Left handed
Propeller rate of revs	134 RPM	134 RPM

flow field due to the presence of the hull is considered. Two propeller designs have been assessed to illustrate the capabilities of the model to distinguish different erosive potential levels originating from the violent collapse of the developed cavities on the blades. The estimated loads and the energy distribution on the blades have been compared to the actual damage on the real blades, highlighting the effectiveness of the presented model and its potential for commercial use already at an early design stage, toward the main goal of higher propulsive efficiency. Such a numerical model could potentially replace model scale cavitation observations in the future.

II. CASE DESCRIPTION

Pressure side cavitation erosion on the blades behind a Ro–Ro container vessel is assessed. This vessel was investigated during a Joint Industry Project followed by the EU-sponsored EROCAV project.[20] Table I shows the main characteristics of the ship depicted in Fig. 1. First, the ship operated with propeller design 1, which experienced severe pressure side cavitation erosion. Then, propeller design 2 was taken from a sister ship and was mounted on the vessel. Full-scale observations were performed only for design 2, confirming the presence of pressure side cavitation at a vessel speed of 13.5 knots. At higher speeds, much less cavitation erosion was observed. Table II shows the particulars of the two designs.

The vessel has mainly been operating in two conditions, the design speed of 19 knots (11450 kW Power), and a lower speed of 13.5 knots and lower power (5930 kW), and both designs seem to suffer from cavitation erosion on the pressure side. To confirm that, calculations were made for both designs and both conditions using the lifting surface program MPUF-3A (mid-chord cavity detachment—propeller unsteady flow). MPUF-3A solves the potential flow around the propeller using the vortex lattice method (VLM). The erosion criterion that was developed within EROCAV project[20] has been applied to all cases where pressure side cavitation is calculated. From the MPUF-3A results, it appeared that design 1 exhibits much more pressure side cavitation as well as higher erosion risk than design 2. While the calculations showed sufficient pressure side cavitation for both ship speeds (13.5 and 19 knots) for design 1, very little pressure side cavitation was predicted on design 2 at 19 knots, aligning very well with the full-scale observations. Thus, in this study, both designs have been simulated at the low-speed condition (13.5 knots) (Fig. 2).

Figure 3 illustrates the erosion damage on the actual blades of design 1 (from operating on the presented vessel) and design 2 (after operating on a sister vessel). Based on these snapshots, design 1 shows less severe damage on the pressure side, even though based on the MPUF-3A calculations, it is expected to have larger amount of pressure side cavitation as well as higher erosion risk on the blades. This can be explained by the fact that the operation time after which these snapshots were captured is unknown. In addition to that, the blades of design 1 have been repaired often. During these repairs, the eroded surfaces were ground out. It should also be noted that the depicted erosion pattern on design 1 is probably due to a combination of operating conditions, since it exhibits pressure side cavitation during a wider range of speeds. On the other hand, design 2 was taken from a sister vessel, which is more likely that she has sailed for longer periods

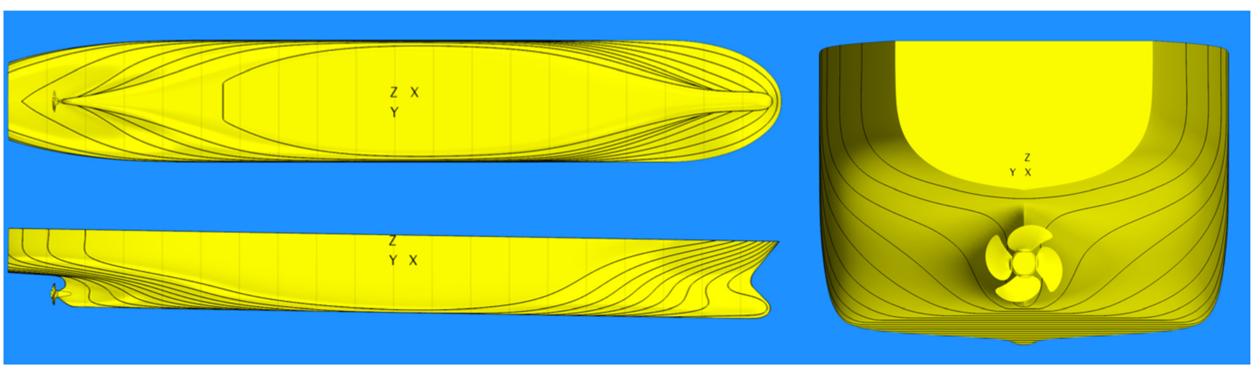

FIG. 1. Hull geometry.

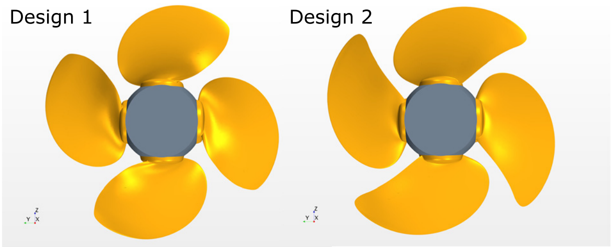

FIG. 2. Propeller designs.

at a relatively low power. It is therefore difficult to compare the erosion extent on these blades from those two snapshots.

III. WETTED FLOW

A. Numerical modeling

The unsteady Reynolds-averaged Navier–Stokes (U-RANS) equations are solved for the fluid motion, using the commercial solver StarCCM+ 13.04.

$$\frac{\partial(\rho \mathbf{u})}{\partial t} + \nabla \cdot (\rho \mathbf{u} \otimes \mathbf{u}) = -\nabla p + \rho f + \nabla \cdot \tau, \tag{1}$$

$$\frac{\partial \rho}{\partial t} + \nabla \cdot (\rho \mathbf{u}) = 0, \tag{2}$$

where $\mathbf{u}$ is the velocity tensor, ρ is the fluid density, p is the pressure, f is the external force per unit mass, and τ is the viscous part of the stress tensor. A segregated approach is adopted solving the conservation equations of mass and momentum in a sequential manner combined with the SIMPLE algorithm for pressure–velocity coupling. Second-order implicit time marching is employed together with a second-order upwind convection scheme.

The free surface is modeled using a homogeneous multiphase model, referred to as volume of fluid (VoF) in StarCCM+. The fluid is treated as a single continuum with different phases. At the interface, the two phases share the same velocity (no-slip condition). The density and the turbulent viscosity at the interface is given by the mixture relations

$$\rho = (1-a)\rho_{\text{air}} + a\rho_l \quad \text{and} \quad \mu = (1-a)\mu_{\text{air}} + a\mu_l, \tag{3}$$

respectively, where $0 < a < 1$ is the liquid volume fraction. An additional transport equation is solved to determine the liquid volume fraction in each computational cell

$$\frac{\partial \alpha}{\partial t} + \nabla \cdot (\alpha \mathbf{u}) = 0. \tag{4}$$

High-resolution interface capturing scheme (HRIC) is employed for the discretization of the convective term in Eq. (4) to minimize numerical diffusion, and increase the sharpness of the interface.[43] Based on normalized variable diagram (NVD),[44] the HRIC scheme simplifies the dependence on the CFL condition, while using an increased order of accuracy.[45] The k–ω SST turbulence model is used to close the RANS equations, and to model the Reynolds stress term,[46] together with an empirical model to reduce the turbulent dissipative terms,[47] to avoid any artificial increase in the eddy viscosity at the interface (see Melissaris *et al.*[48]).

The propeller motion is simulated using rigid body motion (RBM) by creating a rotating region that surrounds the propeller. A non-conformal interface (sliding interface) is used to couple the rotating with the static region at each time step. A representation of the size of the rotating region is shown in Fig. 4, while Fig. 5 shows the dimensions of the static domain used for the self-propulsion simulations. A pressure outlet boundary condition is assigned at the outlet and at the bottom boundary. A velocity inlet boundary condition is assigned at the rest of the boundaries.

The mesh consists of trimmed hexahedral cells with a number of local refinements for the bow, the stern, the free surface, and the wake of the vessel, as shown in Fig. 6. Five sets of grids were generated to assess the mesh sensitivity. Table III shows the grid densities, in terms of the smallest cells size of each grid h_i, and the number of cells in the rotating and the static region for each set of grids. A target wall y^+ value of $30 < y^+ < 300$ is aimed. For the propeller, such y^+ values are harder to obtain than for the hull, due to the higher flow accelerations, especially at higher propeller radii. On top of that, achieving such y^+ together with a low aspect ratio in the near-wall prism layer can result in an excessive number of cells in the propeller region. On the other hand, as the Reynolds number increases, the logarithmic range in velocity profiles extends to much higher y^+ values. Therefore, for flows at high Reynolds numbers, higher y^+ values can be allowed. Moreover, the wall functions are used only to identify the right pitch deflection for the operating condition where erosion risk assessment will be performed. In cavitating flow, a low y^+ treatment is applied to properly resolve the viscous sub-layer.

B. Results and grid sensitivity

Resistance simulations have been performed at 13.5 knots to assess the grid sensitivity of the resistance force. A time step size of

FIG. 3. Actual erosion on the blades for design 1 (left) and design 2 (right). The exact period over which each propeller design had been operated to get the depicted erosion damage is unknown.

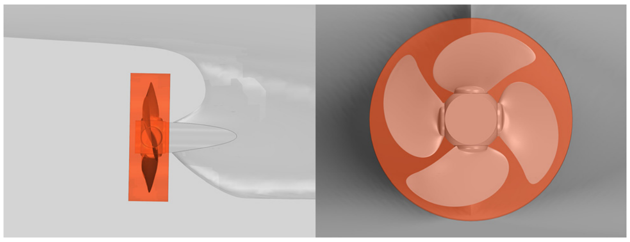

FIG. 4. Representation of the size of the rotating domain.

0.0373 s that corresponds to a propeller rotation rate of 30° per time step has been used in each simulation, which is considered sufficient for all grids, combined with a second-order time marching and a second-order upwind convection scheme. Table IV shows the computed resistance force in all five grids of Table III. Grids 1 and 2 show a difference in resistance more than 2% than the finest grid (grid 5), while grids 3 and 4 give a resistance prediction with a variation lower than 1%. Therefore, grid 3 is considered sufficient for the prediction of the resistance force on the hull.

Additionally, self-propulsion simulations have been performed at the same speed to assess the uncertainty in propeller thrust and torque of design 2. Design 2 was selected for the sensitivity study over design 1, since design 2 was the one fitted on the vessel during the full-scale observations. Figure 7 illustrates the wall y^+ values on the hull and propeller wall surface for grid 3. An average value of $y^+_{avg} \approx 100$ was achieved on the hull, while on the propeller surface, higher values ($y^+_{avg} \approx 540$) are present due to the higher acceleration of the flow, and the propeller motion, as discussed in Sec. III A. propeller rotation rate of 2° per time step has been used in each simulation, which is considered sufficient for all grids, combined again with a second-order time marching and a second-order upwind convection scheme. Looking at the results in Table V, propeller torque is more sensitive to the grid density than thrust. Propeller thrust shows a deviation of less than 1% for all grids apart from the coarsest grid (grid 1), while propeller torque deviates more from the finest grid. However, the torque difference drops below 2% for grids 3 and 4. The generated free surface waves along the hull for grid 3 are illustrated in Fig. 8, showing a quite low wave height. The bow and stern wave heights are also low, indicating that a symmetry plane may be used instead to improve the computational efficiency and stability. Indeed, the results obtained from the double-body (DB) simulation, where the top boundary is at the free surface level, compare very well with the ones obtained with free surface. That indicates that even though the total resistance might be quite different between both simulations, the propeller working point and the propeller inflow seem to be very similar. This observation allows to estimate the erosion risk on the blades by neglecting the free surface effects and therefore increasing the computational efficiency.

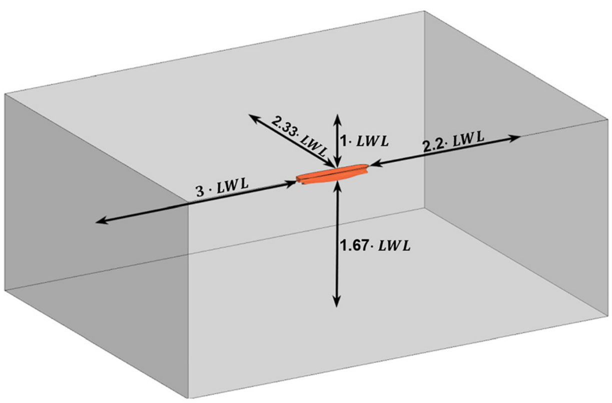

FIG. 5. Dimensions of the numerical domain.

Propulsion simulations have been performed on Grid 3 to estimate the right operating condition for each design. For each propeller design, the performance at four ship speeds has been computed. Tables VI and VII present the results for designs 1 and 2, respectively. Comparing the CFD results for design 2 to the full-scale measurements (only available for design 2), quite some difference is observed on the power absorption at the same ship speed. A higher propeller torque was measured at 13.5 knots ship speed. However, this can be attributed to the fact that no added resistance for the hull and propeller roughness has been considered that could increase the torque absorption significantly. Therefore, using the torque identity to match the measured power would lead to a ship speed quite lower than the trial speed (12.2 knots).

The MPUF-3A results for the thrust coefficient at the measured delivered power of 5930 kW are also presented for both designs. Interpolating to match this thrust leads to a ship speed closer to 13.5 knots for both designs than interpolating to the delivered power of 5930 kW. Even though thrust computation may have a higher uncertainty than the power measurements, it was decided to use the

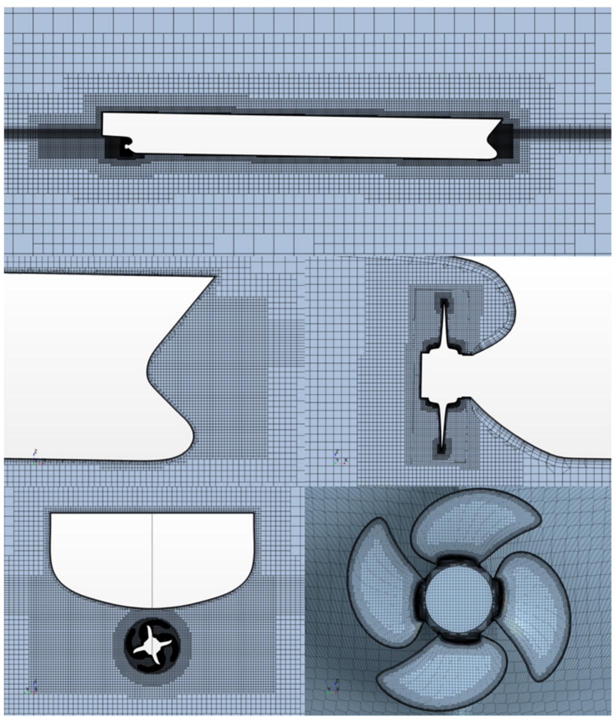

FIG. 6. Representation of the mesh of grid 3 and the refinements on the bow, stern, free surface, and the wake of the hull.

TABLE III. Description of the different generated grids for the wetted flow self-propulsion simulations, showing the smallest cell size of each grid h_i, the grid refinement ratio h_i/h_5, and the number of cells in the static and rotating region.

Grid	h_i	h_i/h_5	No. of cells in rotating region	No. of cells in static region
Grid 1	0.006 61	2.34375	2.55 M	1.80 M
Grid 2	0.005 29	1.5875	3.76 M	2.59 M
Grid 3	0.004 41	1.5625	4.95 M	4.20 M
Grid 4	0.003 53	1.25	5.77 M	6.66 M
Grid 5	0.002 82	1	7.44 M	11.42 M

TABLE IV. Resistance values for five sets of grids with free surface, and for grid 3 using a double-body approach (no free surface).

	Resistance (kN)	% diff.
G1 (VoF)	343.4	4.38%
G2 (VoF)	335.6	2.01%
G3 (VoF)	330.3	0.34%
G4 (VoF)	327.3	−0.58%
G5 (VoF)	329.2	···

TABLE V. Propeller thrust and torque values for four sets of grids with free surface, and for grid 3 using double body approach (no free surface).

	T (kN)	% diff.	Q (kN m)	P (kW)	% diff.
G1 (VoF)	553.4	2.08%	386.0	5417	4.57%
G2 (VoF)	547.2	0.94%	379.1	5319	2.68%
G3 (VoF)	545.5	0.63%	376.1	5278	1.89%
G4 (VoF)	543.1	0.18%	373.4	5240	1.15%
G5 (VoF)	542.1	···	369.1	5180	···
G3 (DB)	544.5	0.443%	375.7	5271	1.79%

thrust identity to get the conditions for the erosion risk analysis. Interpolating to the thrust coefficient as derived from the MPUF calculations leads to a ship speed of 12.8 knots for design 1 and 13.3 knots for design 2. Nevertheless, the difference in the vapor volume and its dynamics for small variations in ship speed did not seem to be very large.

IV. CAVITATING FLOW

A. Cavitation model and computational mesh

The low Froude number (Fr = 0.164) and the low wave resistance at low ship speeds (U = 13.5 kn) allow for neglecting the free surface waves in order to increase computational efficiency in the cavitating

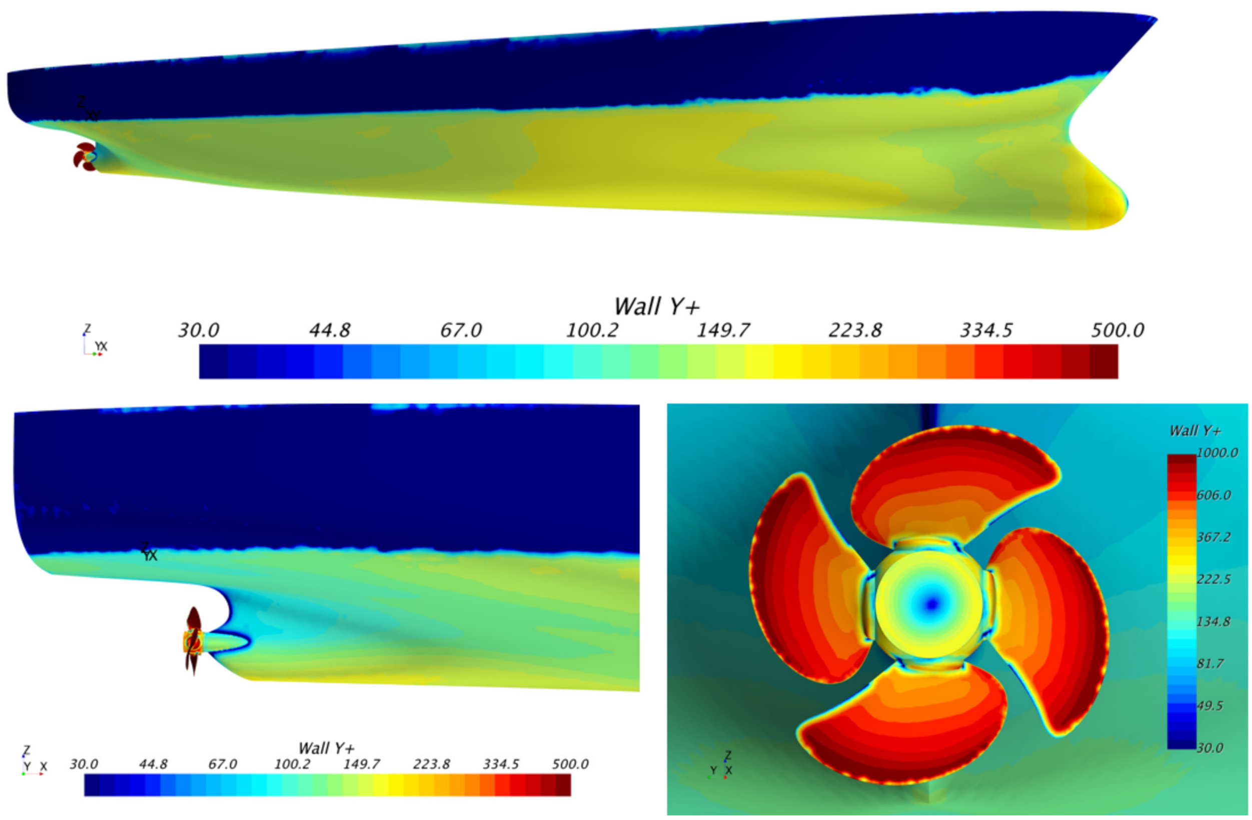

FIG. 7. Wall y^+ values on the hull and the propeller wall surface for grid 3.

flow simulations. This is done by replacing the free surface by a symmetry boundary condition at the free surface level. In that case, the air phase is neglected and it is replaced by the vapor phase in the solver, so that the mixture relations become

$$\rho = a_v \rho_v + (1 - a_v)\rho_l \quad \text{and} \quad \mu = a_v \mu_v + (1 - a_v)\mu_l, \tag{5}$$

respectively, where $0 < a_v < 1$ is now the vapor volume fraction. An additional source term is added on the r.h.s. of Eq. (4) to model the mass transfer between liquid and vapor

$$\frac{\partial \alpha_v}{\partial t} + \nabla \cdot (\alpha_v \mathbf{u}) = S_{\alpha_v}, \tag{6}$$

where S_{α_v} is the mass transfer source term as defined by the Schnerr–Sauer cavitation model.[49] The pure phases are treated as incompressible, and compressibility is mimicked only in the mixture regime. The high ambient pressures (≈1 bar) result in an inertia-driven flow and the mass transfer model can give realistic predictions as long as the density–pressure trajectories are steep enough. The steepness of the density–pressure trajectory is controlled by the

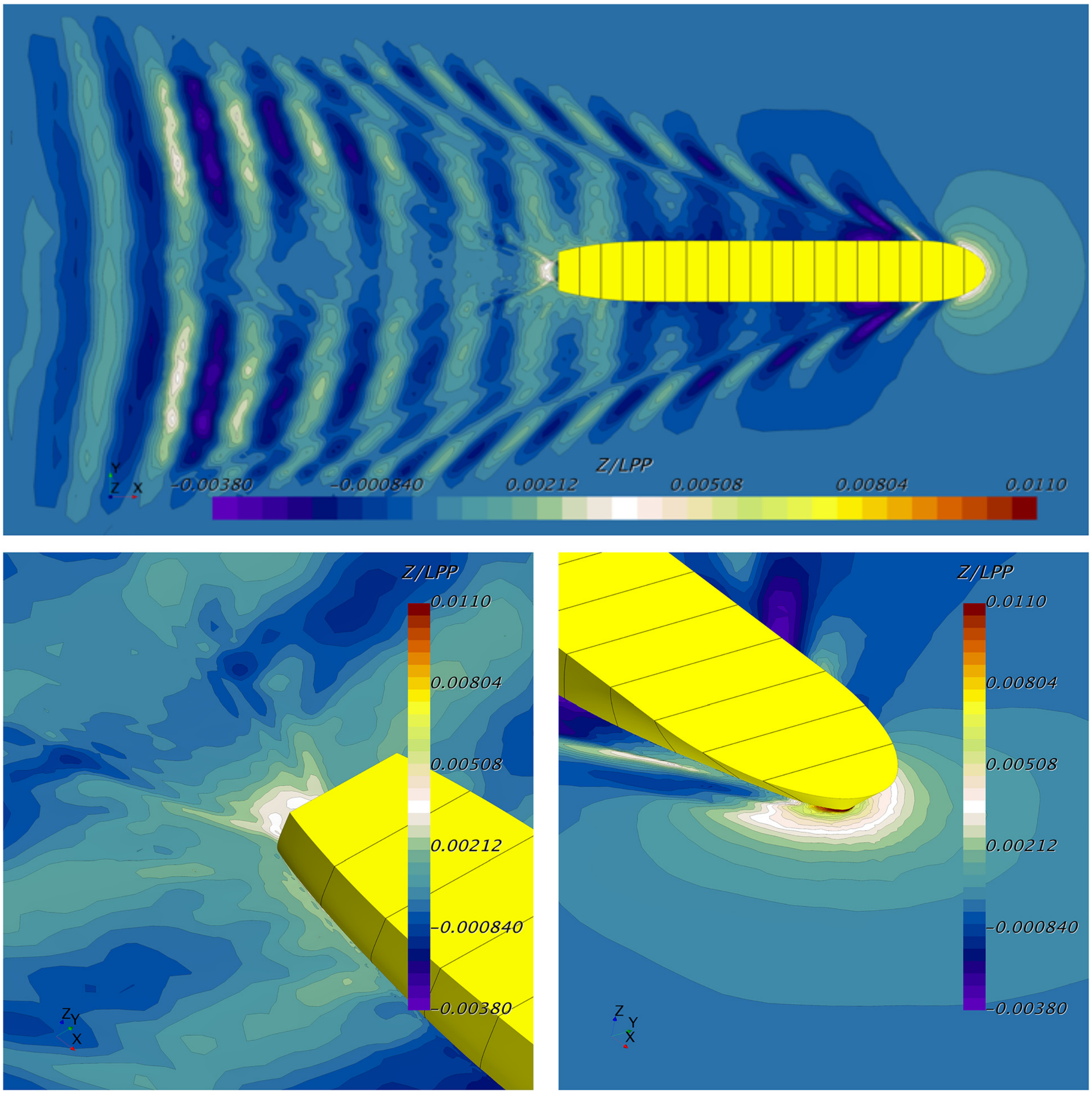

FIG. 8. Representation of the free surface waves.

TABLE VI. Propeller thrust and torque values for different ship speeds for design 1 on grid 3.

Ship speed (kn)	T (kN)	K_T (-)	Q (kN m)	K_Q (-)	P (kW)
12.5	471.0	0.094	412.4	0.015	5787.3
13.0	427.6	0.085	400.0	0.014	5613.0
13.5	382.9	0.076	386.9	0.014	5429.5
14.0	338.1	0.067	373.7	0.013	5244.0
13.5 (MPUF-3A)		0.088			5930

evaporation and condensation coefficients of the mass transfer source term[40,41] that should be large enough (equal or larger than 1) to enforce a quick transition from vapor to liquid phase and vice versa. In this study, both coefficients are set equal to 1, which even though is at the limit, it gave the best convergence behavior.

TABLE VII. Propeller thrust and torque values for different ship speeds for design 2 on grid 3.

Ship speed (kn)	T (kN)	K_T (-)	Q (kN m)	K_Q (-)	P (kW)
12.0	678.6	0.135	429.3	0.015	6027.7
12.5	636.8	0.127	412.8	0.015	5792.7
13.0	593.8	0.118	395.6	0.014	5551.3
13.5	544.5	0.108	375.7	0.013	5271.3
13.5 (measured)					5930
13.5 (MPUF-3A)		0.112			5930

TABLE VIII. Mesh information after the applied volume refinement on one of the blades, showing the total number of volume cells, surface cells on the refined blade, prism layers, and cells per cavity width along the maximum cavity size.

	Total no. of cells	No. of cells Refined blade	No. of prism Layer cells	No. of minimum cells Per cavity width
D1	10.1 M	126 k	16	25
D2	18.5 M	303 k	16	25

For the cavitation erosion risk analysis, the mesh needs to be adjusted. A volume refinement is applied around one of the blades and on the volume cells where the vapor volume has a non-zero value over one full propeller revolution. Based on the best practice guidelines from previous studies,[41,42] approximately 20–25 cells (excluding the prism layer cells) along the smallest dimension of the vapor cavity, when it is at its maximum size, are used, as well as about 40 time steps during the collapse, based on the Rayleigh–Plesset collapse time.[2] Figure 9 shows the approximate maximum size of the developed sheet cavity, before it starts to shed, for designs 1 and 2, respectively. Regarding design 1, for a cavity with diameter $D \approx 125$ mm, this translates to a minimum cell size of $c \approx 5$ mm, and a time step size of $\Delta t = 1.45 \times 10^{-4}$ s or a rotation rate of 0.12° per time step. To keep the cell size of the refinement a perfect multiple of the background mesh, eventually, a cell size $c \approx 4.4$ mm has been selected for the refinement that corresponds to at least 25 cells per cavity width at any time instant. The chosen time step size is $\Delta t = 1.28 \times 10^{-4}$ s or a rotation rate of 0.1° per time step, corresponding to about 45 time steps during the collapse. Design 2 appears to have a cavity size on the blade that is roughly half the size of the one on design 1. Therefore, half the cell size

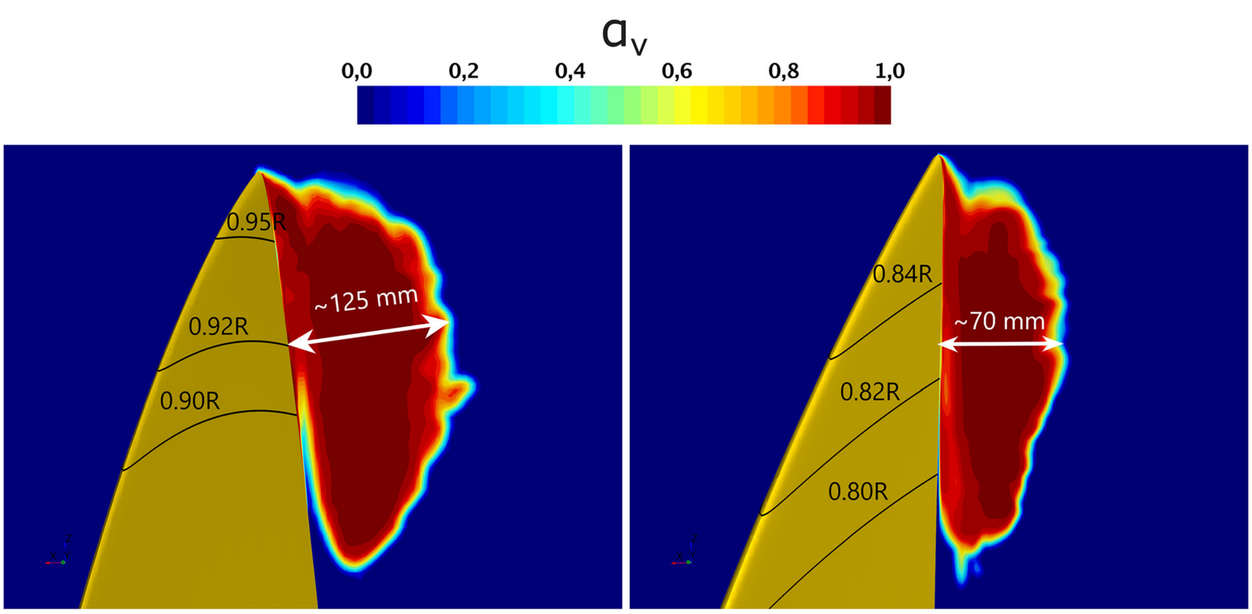

FIG. 9. Representation of the vapor volume at an arbitrary radial section, showing the approximate maximum size of the developed sheet cavity, before it starts to shed, over one revolution for design 1 (left) and design 2 (right).

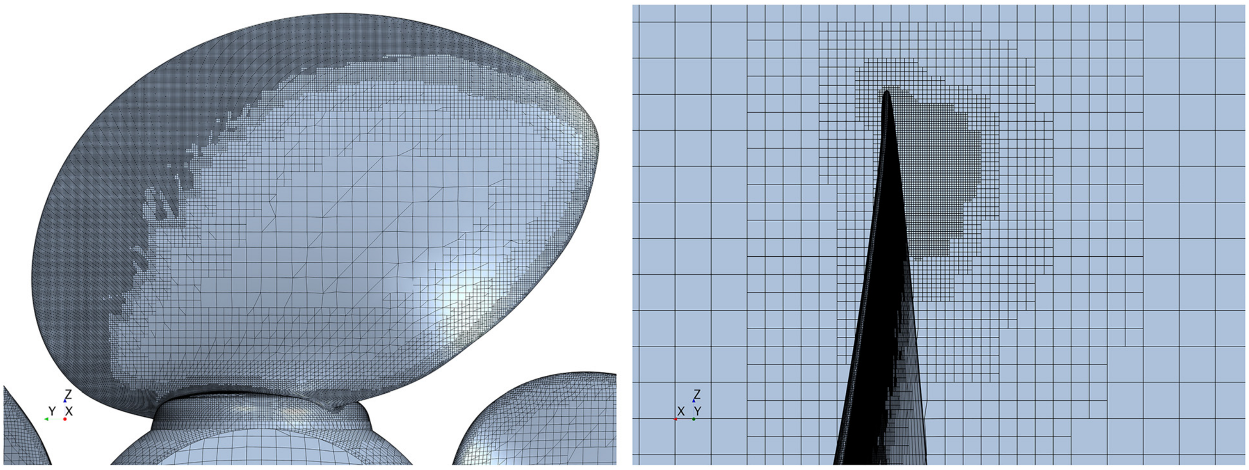

FIG. 10. Representation of the mesh on the refined blade of design 1.

has been selected for the volume refinement ($c \approx 2.2$ mm) and the time step size ($\Delta t = 0.64 \times 10^{-4}$ s or a rotation rate of 0.05° per time step), so that the same amount of cells are used along the cavity and the same number of time steps during the collapse.

A high wall resolution is required to correctly capture the cavitation on the blade,[23,50] but also to get a good transition between the prism layer and the volume cells. The wall y^+ values should be well below 1 (≈ 0.1) for high-fidelity predictions, especially when the k–ω SST turbulence model is used to model Reynolds stresses.[51] Achieving such low y^+ values normally leads to a much larger number of prism layer cells, to avoid a bad transition between the prism layer and the volume cells, increasing the total mesh size significantly. Table VIII shows the eventual number of cells in the domain, on the blade and in the prism layer region, while Figs. 10 and 11 illustrate the refined mesh on design 1 and design 2, respectively. The obtained wall y^+ values on the blade surface for each design are depicted in Fig. 12. The average y^+ value over the refined blade is very similar for both designs, $y^+ = 0.41$ for design 1 and $y^+ = 0.42$ for design 2. Lower y^+ values would be desirable, but would lead to a larger number of prism layer cells that could increase the total number of cells significantly. Therefore, a compromise is made for somewhat larger y^+ values (still much lower than 1), but we ensure a better mesh quality, and computational efficiency.

B. Cavitation erosion modeling

The cavitation implosion loads are predicted using an energy balance approach, where the initial cavity potential energy is proportional to the cavity volume and the difference between the driving pressure, p_d, and the pressure within the cavity, p_v,

$$E_{\mathrm{pot},0} = (p_d - p_v) \cdot V_v. \tag{7}$$

During the collapse, the potential energy is converted into kinetic energy, while it is being focused on the collapse center. At the

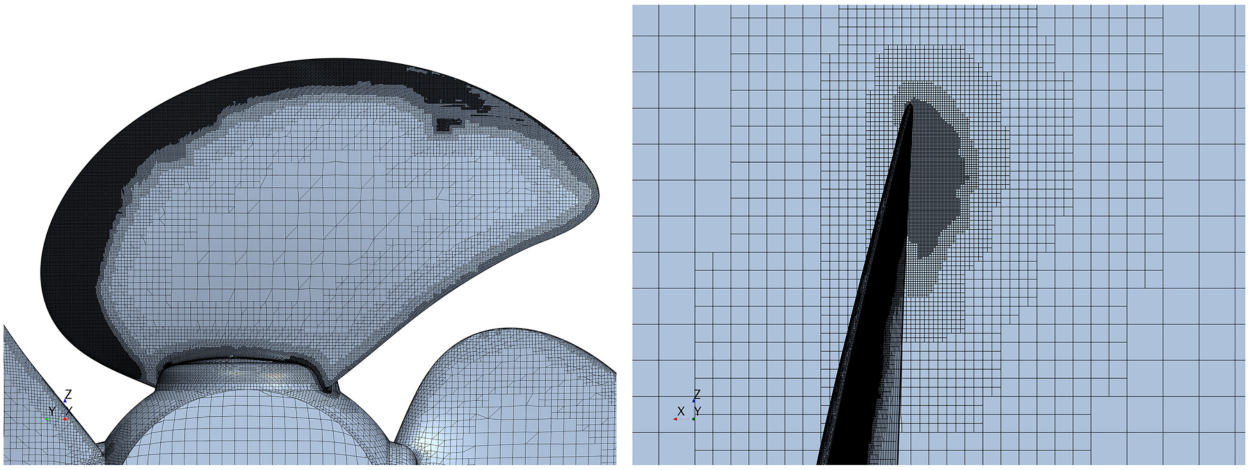

FIG. 11. Representation of the mesh on the refined blade of design 2.

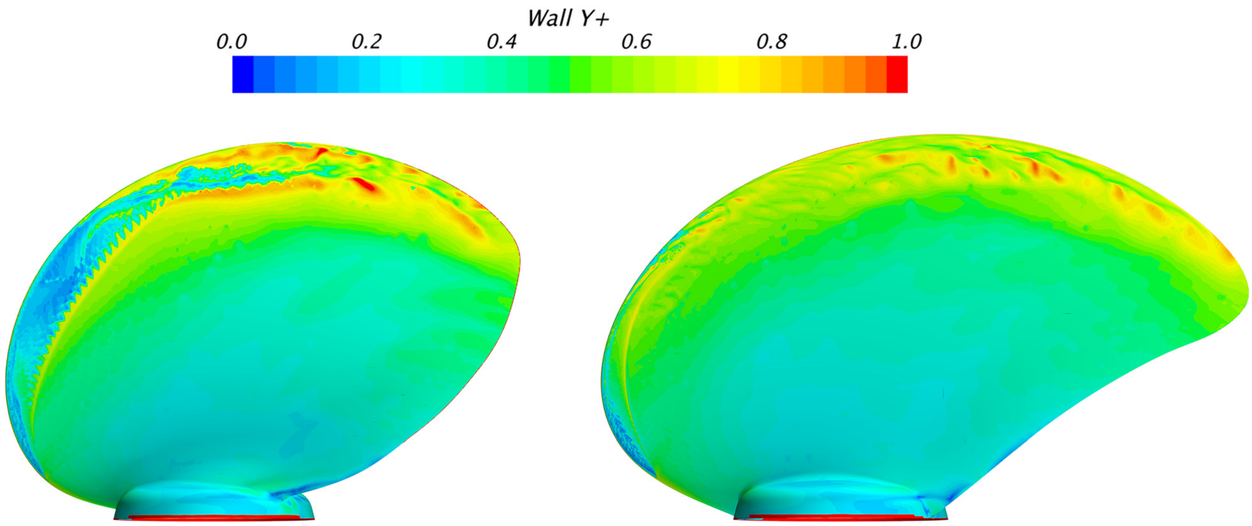

FIG. 12. Wall y^+ values on the surface of the refined blade of designs 1 (left) and 2 (right) when the blades are at the top position.

final stage of the collapse, it is assumed that all the kinetic energy is converted into acoustic radiated energy, E_{SW} (neglecting rebound, E_{reb}, and thermal effects, ΔU), justified by the relatively high driving pressures and the absence of non-condensable gas in the flow[52]

$$E_{SW} = E_{\text{pot},0} - E_{\text{reb}} - \Delta U \underset{\Longleftrightarrow}{E_{\text{reb}} \approx 0,\, \Delta U \approx 0} E_{SW} \approx E_{\text{pot},0}. \tag{8}$$

The change of potential energy in each volume cell with volume, V_{cell}, is computed by the material derivative of the potential energy, E_{pot}, such that

$$\dot{e}_{\text{pot}} = \frac{DE_{\text{pot}}/Dt}{V_{\text{cell}}} = (p_d - p_v) \cdot \frac{D\alpha_v}{Dt}, \tag{9}$$

where the material derivative of the driving pressure has been omitted, as it does not contribute to energy radiation from the imploding cavities.[40,41] The material derivative of the vapor volume fraction a_v is computed from the mass transfer source term, while only condensation is considered.[41] Combining Eq. (2), (3), and (6) gives

$$\dot{e}_{\text{pot},C}(t, \mathbf{x}_{\text{cell}}) = (p_d - p_v)\cdot\min\left[\frac{\rho}{\rho_l} S_{\alpha_v}, 0\right]. \tag{10}$$

The driving pressure, $p(d)$, involves the highest uncertainty in defining the potential energy content in cavitating flows. In complex cavitating flows, the driving pressure is typically unknown and at the same time highly unsteady and non-uniform. To get an approximation of the conditions to which arbitrary-shaped cavitating structures are subjected, the moving average of the instantaneous pressure $p(t)$,

$$p_d(t) = \frac{1}{T_m}\int_{t-T_m}^{t} p(t)dt, \tag{11}$$

is used as driving pressure. The sliding window T_m should be equal to at least one shedding cycle.[40,41] To avoid exceeding random-access memory (RAM) limits, the moving average is approximated by the method introduced by Welford,[53] which gives

$$p_d(t) = p_d(t - \Delta t) + [p(t) - p_d(t - \Delta t)]\frac{\Delta t}{T_m}, \tag{12}$$

where Δt is the time step size. The proposed driving pressure allows to capture the effect of pressure recovery gradients on statistical average. An alternative approach to tackle the uncertainty of the driving pressure field is proposed by Arabnejad *et al.*,[28] where the energy description of cavitation erosion is based on the kinetic energy of the surrounding liquid during the collapse, instead of the potential energy. In this way, the driving pressure does not need to be derived. However, the whole approach is based on a different framework, and since it is not based on the initial potential energy of collapsing cavities, the energy conservation can be hard to monitor and control.

The surface accumulated energy is predicted with and without energy focusing to illustrate once more the capabilities of the energy focusing approach. In the case where no focusing is applied, then the radiated power, $\dot{e}_{\text{rad}}$, is directly coupled to the negative change of potential energy during condensation from Eq. (10)

$$\dot{e}_{\text{rad}}(t, \mathbf{x}_{\text{cell}}) = -\dot{e}_{\text{pot},C}(t, \mathbf{x}_{\text{cell}}). \tag{13}$$

On the other hand, when energy focusing is applied, a transport equation is implemented for the collapse-induced kinetic energy ε, as introduced by Schenke *et al.*[54]

$$\frac{\partial\varepsilon}{\partial t} + \mathbf{u}_i \cdot \nabla\varepsilon = -\varepsilon(\nabla \cdot \mathbf{u}_i) - \dot{e}_{\text{rad}}(t), \tag{14}$$

where $\mathbf{u}_i$ is the collapse-induced velocity. The two terms on the r.h.s. of Eq. (14) represent the generation of kinetic and radiated energy, respectively. The term $\mathbf{u}_i \cdot \nabla\varepsilon$ is responsible for the conservative transport of the collapse-induced kinetic energy ε. However, the distribution of ε around the cavity interface during the collapse process is unknown, as it is difficult to distinguish the collapse-induced velocities from the inertial flow velocities derived from the solver. Therefore, a modeling assumption is introduced[40,41,54] and the collapse-induced kinetic energy can be computed as follows:

$$\frac{\partial \varepsilon}{\partial t} = \underbrace{(1-\beta)\left[\phi(\varepsilon) - \dot{e}_{\mathrm{pot},C}(t)\right]}_{\text{kinetic energy flux}} - \underbrace{\beta \dot{e}_{\mathrm{rad}}(t)}_{\text{radiated energy flux}} . \quad (15)$$

In Eq. (15), $\phi(\varepsilon)$ represents the modeling for the advective transport of the collapse-induced kinetic energy ε, and it can be decomposed into a production and a reduction term, such that the amount of the transported energy is conserved. For that, the transport term should satisfy

$$\int_V \left[\phi(\varepsilon)^+ + \phi(\varepsilon)^-\right] dV = 0. \quad (16)$$

It is assumed that the reduction term $\phi(\varepsilon)^-$ is proportional to ε to ensure that $\varepsilon \geq 0$ and that the fraction of ε reduced by $\phi(\varepsilon)^-$ per time δt is given by the normalized projection of $\nabla\varepsilon$ on the local flow velocity $\mathbf{u}$. The reduction term is then defined as

$$\phi(\varepsilon)^- = -\frac{\varepsilon}{\delta t}\mathfrak{P}_u(\nabla\varepsilon), \quad (17)$$

and the projection operator is given by

$$\mathfrak{P}_u(\nabla\varepsilon) = \max\left[\frac{\mathbf{u}}{||\mathbf{u}||}\cdot\frac{\nabla\varepsilon}{||\nabla\varepsilon||}, 0\right]. \quad (18)$$

Since the distribution of ε is unknown, the collapse-induced kinetic energy is stored at the cavity interface. The flow at the interface is directed toward the collapse center, and therefore, it is aligned with $\nabla\varepsilon$.

The formulation of the production term is driven by the assumption that the collapse-induced kinetic energy is generated at locations where there is a negative change of potential energy. Thus, the production term should be proportional to $\dot{e}_{\mathrm{pot},C}(t)$, such that

$$\phi(\varepsilon)^+ = -k\dot{e}_{\mathrm{pot},C}(t, \mathbf{x}_{\mathrm{cell}}), \quad (19)$$

where k is constant in space and is determined by

$$k = \begin{cases} \dfrac{\int_V \phi(\varepsilon)^- dV}{\int_V \dot{e}_{\mathrm{pot},C}(t) dV} & \text{for } \dot{e}_{\mathrm{pot},C} < 0, \\ 0, & \text{elsewhere,} \end{cases} \quad (20)$$

so that energy conservation is ensured. Then, Eq. (15) becomes

$$\frac{\partial \varepsilon}{\partial t} = (1-\beta)\left[\dot{e}_{\mathrm{pot},C}(t)(k-1) - \frac{\varepsilon}{\delta t}(\mathfrak{P}_u(\nabla\varepsilon))\right] - \beta\dot{e}_{\mathrm{rad}}(t). \quad (21)$$

The blending factor β is responsible for identifying the final collapse stage and therefore the conversion of the collapse-induced kinetic energy into radiated acoustic energy. Its formulation is motivated by the assumption that after the collapse, the volume cell should consist only of liquid. Furthermore, the pressure in the mixture regime cannot be much higher than the vapor pressure, and consequently, a high-amplitude pressure wave can only form in the liquid phase. That gives

$$\beta = \begin{cases} 1, & \text{if} \quad p > p_\infty \quad \text{and} \quad \alpha = 0, \\ 0, & \text{else.} \end{cases} \quad (22)$$

When $\beta = 0$, the collapse-induced kinetic energy keeps increasing and being focused toward the collapse center, while when $\beta = 1$, the accumulated kinetic energy at the collapse center will be radiated to the domain.

The solution of Eq. (21) is explicitly forwarded in time using a first-order Taylor expansion, by the time increment δt, which can be replaced by the time step size Δt

$$\varepsilon^*|_{t+\Delta t} = \left[\dot{e}_{\mathrm{pot},C}\Delta t(k-1) - \varepsilon(\mathfrak{P}_u(\nabla\varepsilon) - 1)\right]|_t. \quad (23)$$

The blending factor β is applied at the same time level $t + \Delta t$ to both the kinetic energy flux ($\beta = 0$) and the radiated energy flux ($\beta = 1$) to ensure energy conservation. That gives

$$\varepsilon|_{t+\Delta t} = (1 - \beta|_t)\varepsilon^*|_{t+\Delta t} \quad (24)$$

for the collapse-induced kinetic energy, and

$$\dot{e}_{\mathrm{rad}}|_{t+\Delta t} = \beta\frac{\varepsilon^*|_{t+\Delta t}}{\Delta t} \quad (25)$$

for the radiated power. By integrating over all the radiation sources, the impact power per unit surface at any location $\mathbf{x}_S$ can be computed, such that

$$\dot{e}_S(t, \mathbf{x}_S) = \frac{1}{4\pi A_f}\int_V \Omega_d\, \dot{e}_{\mathrm{rad}}(t, \mathbf{x}_{\mathrm{cell}}) dV, \quad (26)$$

where

$$\Omega_d = \min\left[\left(\frac{(\mathbf{x}_{\mathrm{cell}} - \mathbf{x}_S)\cdot\mathbf{n}}{||\mathbf{x}_{\mathrm{cell}} - \mathbf{x}_S||^3}A_f\right), 2\pi\right] \quad (27)$$

is the discrete solid angle,[41] and A_f is the surface cell face area.

Since the energy radiation in the present study is done in a discrete way at each time step, and the exact energy distribution is unknown, a statistical approach is applied to distinguish between extreme events and repetitive events of low amplitude. The identification of the extreme events is based on the idea to amplify the surface impact power by an intensity component in Ref. 40, which is achieved by the power or Hölder mean, given by

$$M_{\{n\}}(\dot{e}_S) = \left(\frac{1}{T}\int_T (\dot{e}_S(t, \mathbf{x}_S))^n dt\right)^{\frac{1}{n}}. \quad (28)$$

As the intensity parameter n increases, the power mean approaches the amplitude of the input signal $\dot{e}_S$. Equation (28) requires that the energy projection to the surface takes place during each time step. Since the surface projection is computationally not very efficient, the intensity component n is applied in a modified way, so that the energy projection can be performed at any time instant, for instance, at the end of each propeller revolution. That gives

$$M_{\{n\}}(\dot{e}_S(\mathbf{x}_S)) = \left(\frac{1}{TV}\int_T\int_V (\dot{e}_S(t, \mathbf{x}_S))^n dV dt\right)^{\frac{1}{n}}, \quad (29)$$

and since the solid angle Ω_d is not time-dependent, the time and volume integrals can be interchanged, so that the volume integration is performed only once at the end of the time integration

$$M_{\{n\}}(\dot{e}_S) = \left(\frac{1}{TV}\frac{1}{4\pi A_f}\int_V \Omega_d^n \int_T (\dot{e}_{\mathrm{rad}})^n dt dv\right)^{\frac{1}{n}}. \quad (30)$$

The amplified impact power from Eq. (30) is used to construct a filter that attenuates the contribution of low-amplitude events, so that extreme events can be identified. Following the work by Schenke,[40] the filter $F_{\{n\}}$ is derived by normalizing the amplified impact power distribution by its maximum value, such that

$$F_{\{n\}} = \frac{M_{\{n\}}(\dot{e}_S)}{\max\left[M_{\{n\}}(\dot{e}_S)\right]}, \quad \text{where} \quad F_{\{n\}} \in [0,1]. \tag{31}$$

Then, the filtered surface energy distribution is given by

$$e_{S_{\{n\}}} = e_S F_{\{n\}}, \quad \text{where} \quad e_S = \int_0^T \dot{e}_S(t, \mathbf{x}_S) dt. \tag{32}$$

The filtering procedure is done after each propeller revolution. Finally, the filtered average impacted power after a certain amount of revolutions can be computed by

$$\dot{e}_{S_{\{n\}}} = \frac{e_{S_{\{n\}}}}{iT_i}, \tag{33}$$

where i is the number of propeller revolutions, and T_i is the time for each revolution.

A convergence criterion, r, is employed to ensure the iterative convergence during each time step. The criterion is satisfied when the deviation between the maximum and the minimum value of the total vapor volume fraction, α_v, over the last n iterations, divided by the average of α_v over the last n iterations is lower than 10^{-6}

$$r = \frac{\left|\max\{\alpha_v\}_{j=i-n+1}^{i} - \min\{\alpha_v\}_{j=i-n+1}^{i}\right|}{\frac{1}{n}\sum_{j=i-n+1}^{i} \alpha_{v_j}} < 10^{-6}, \tag{34}$$

where $i \geqq 5$ is the iteration number during the time step. A value $n = 5$ is set in the simulations, together with a number of maximum inner iterations equal to 100 for design 1 and 50 for design 2 (the smaller time step size allows for half the maximum inner iterations during each time step).

C. Erosion risk assessment

The erosion risk on the propeller blades of designs 1 and 2 has been assessed for five propeller revolutions. The pressure distribution on the blades, as a result of the moving average of the instantaneous pressure over one propeller revolution, is shown in Fig. 13. The pressure recovery gradient is more pronounced for design 1, and thus, more violent collapses should be expected, considering also the larger vapor volume on the blades, as shown in Fig. 14. Design 2 has less vapor volume on the blades, but it fluctuates a lot during each propeller revolution. FFT analysis on the vapor volume history of both blades identifies the same main frequencies around the BPF. However, for design 2 some higher frequencies can be seen, correlating well with the dynamic behavior of the vapor volume (Fig. 15). This might indicate a high-frequency shedding on the pressure side of the blade, resulting in multiple implosions during each revolution. A closer look at the vapor volume dynamics may confirm this assumption.

Figure 16 depicts the instantaneous vapor volume on the pressure side of propeller design 1, when the propeller is located at 0°, 90°, 180°, and 270° position. A sheet cavity is formed at the leading edge, which appears to be quite stable at low radii during a full revolution. The sheet cavity extends approximately until 70%–80% of the propeller radius, at which point dynamic shedding occurs. At higher radii, a reentrant jet is present, and the cavity starts to shed. Due to the high vorticity in the flow, the shed cavities seem to roll up together, forming a thick vortex above the blade surface, which extends until the mid-chord of the blade, or even a bit further. Cloudy structures detach from the vortex and collapse independently. The same process is taking place continuously during a full revolution, until the blade approaches the top position. As the blade passes through the wake

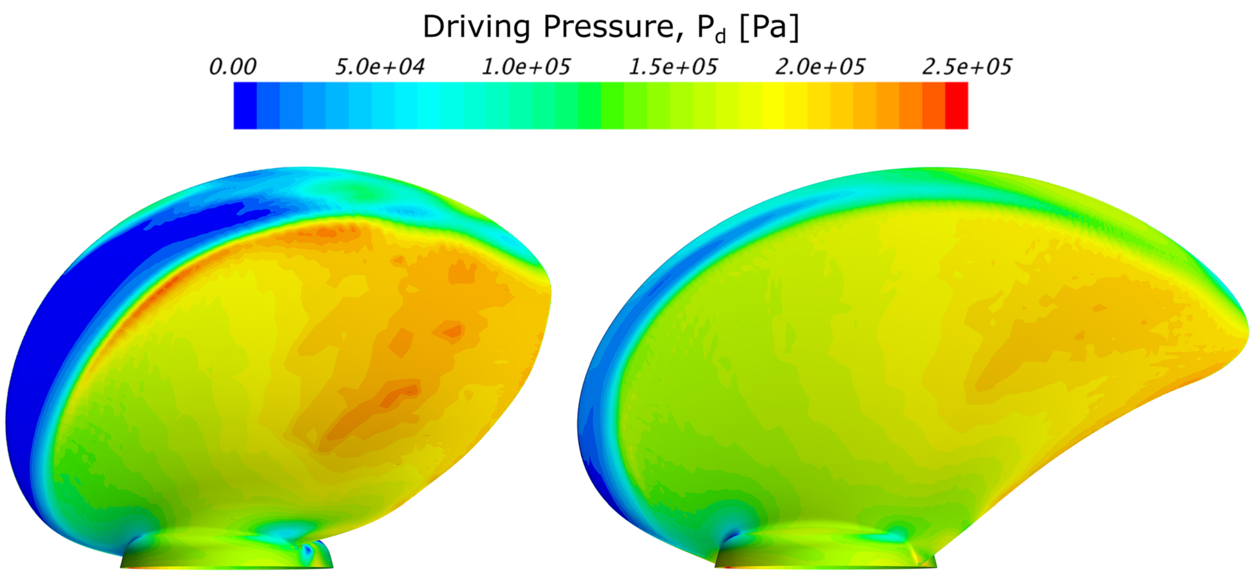

FIG. 13. Time-averaged pressure distribution on the surface of the refined blade of design 1 (left) and 2 (right) after a sample time of one propeller revolution. A pronounced pressure gradient is observed over the cavitation free region of the blade.

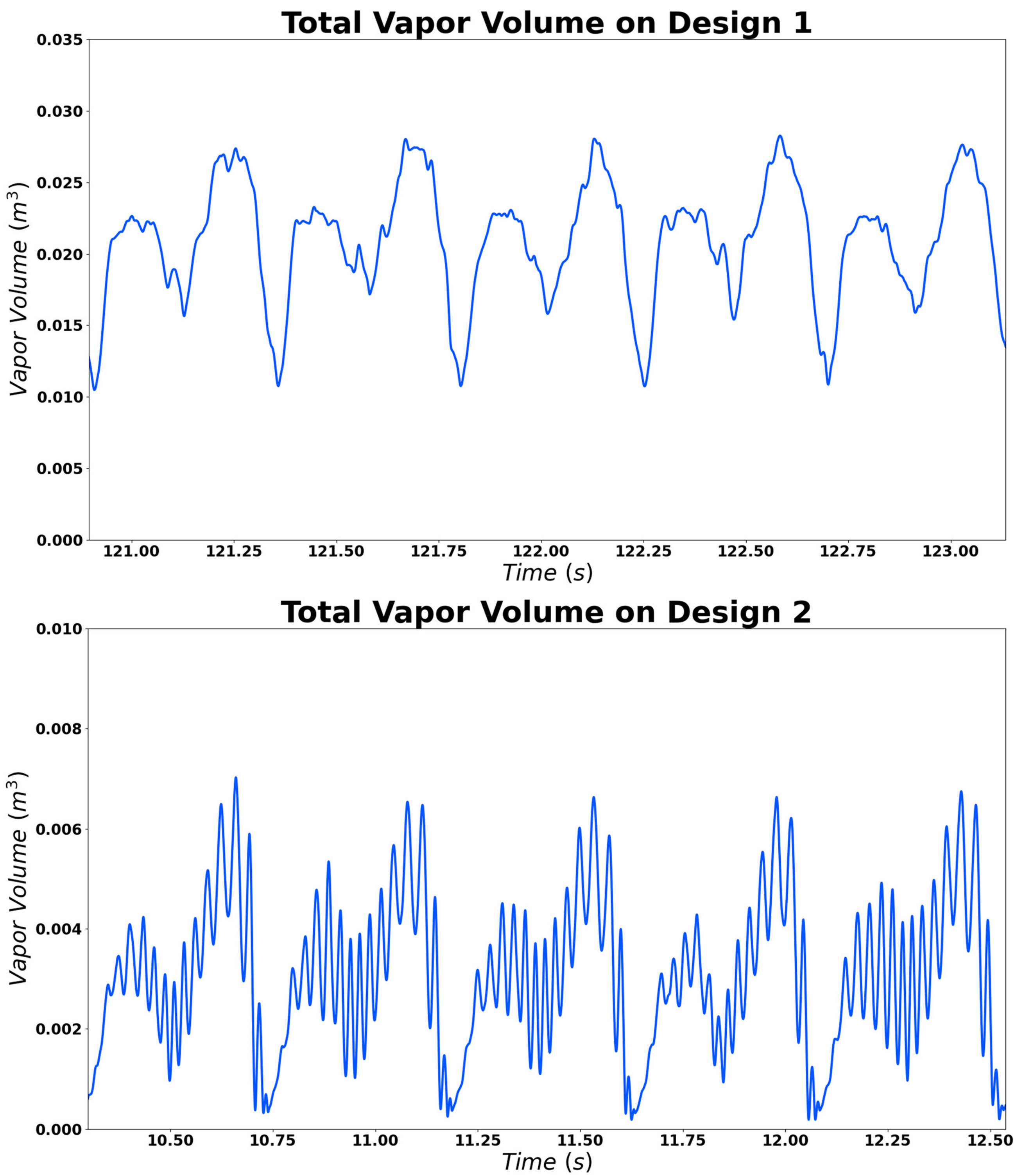

FIG. 14. Total vapor volume development in time for design 1 (top) and design 2 (bottom) for five propeller revolutions.

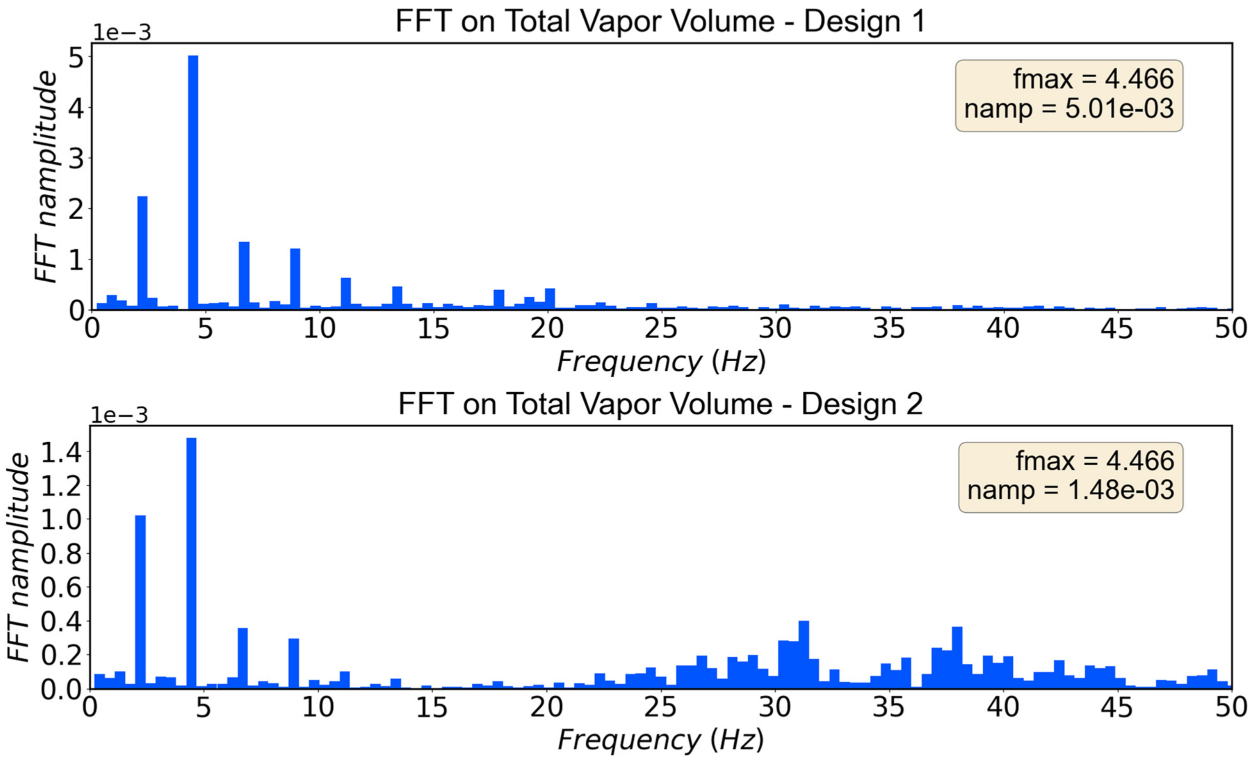

FIG. 15. Spectral analysis of the total vapor volume for design 1 (top) and design 2 (bottom).

peak, a more violent event is observed. Figure 17 presents the instantaneous vapor volume development around the top blade position. As the blade passes the top position, the sheet cavity gets thinner, while the cavitating structures shown within the red circle at 352° position collapse close to the tip around the mid-cord of the blade. When the blade is at 12° position, only a small amount of vapor is still present at this location, which will eventually collapse as well. This event is hypothesized to produce the highest implosion loads during each propeller revolution. Unfortunately, the erosion risk assessment is a rather computationally expensive process, and it is not performed during each time step, but at the end of each revolution. Therefore, we cannot follow the distribution of the radiated energy in time.

The main shedding frequency of design 2 is the same as design 1 (equal to the BPF). However, design 2 shows slightly different cavitation dynamics, as it experiences shedding also at much higher frequencies, as indicated by the FFT analysis on the vapor volume time series. Looking at the instantaneous vapor volume at various blade positions (see Fig. 18), the developed sheet cavity on the blade is much smaller than the one in design 1. The smaller size of the sheet cavity is associated with the weaker pressure gradient on the blade (see Fig. 13). A closer look on the vapor volume development during each revolution illustrates two different collapse events on the blade surface. First, shedding of the sheet cavity occurs at a much higher frequency than the BPF, as depicted in Fig. 19. An example of the sheet cavity is shown at 285° blade position. The sheet cavity slowly separates from the blade leading edge due to a re-entrant jet that travels toward the leading edge. At 300° blade position, the sheet cavity has already shed into a cloudy structure. Part of the cavity rolls up into a cavitating vortex that extends toward the mid chord of the blade, similar to the one shown for design 1, although with much lower volume. A new sheet cavity is developed (305° blade position) and the cloudy structure that is separated from the vortex quickly collapses (310° blade position), while the sheet cavity grows back to its initial size. This process takes place multiple times during each revolution, with a shedding frequency between 25 and 45 Hz (see Fig. 15). The generated vortex shows a similar dynamic behavior as in design 1. Nevertheless, its core remains rather constant during a full propeller revolution, until the blade approaches the top position. Looking at the vapor volume of the upcoming blade, as shown in Fig. 20, the cavitating vortex slowly collapses close to the mid-chord of the blade, as it passes from the 305° position and gets closer to the top position. The collapse process has a lower frequency (occurs once per propeller revolution on each blade), and it is slower than the one occurring at lower radii, and at a higher frequency.

Figure 21 presents the total accumulated energy on the refined blade for each design, during each propeller revolution, without and with energy focusing. Even though the total accumulated energy is not directly related to the erosion risk levels, very often higher accumulated energy translates to higher erosion risk. The surface energy distribution and the energy density on the blades can possibly give more information about the aggressiveness of the implosion loads on the surface. From Fig. 21, the accumulated energy on the blade surface of design 1 is almost two times larger than on design 2. Moreover, we observe that for design 1, higher energy is predicted without energy

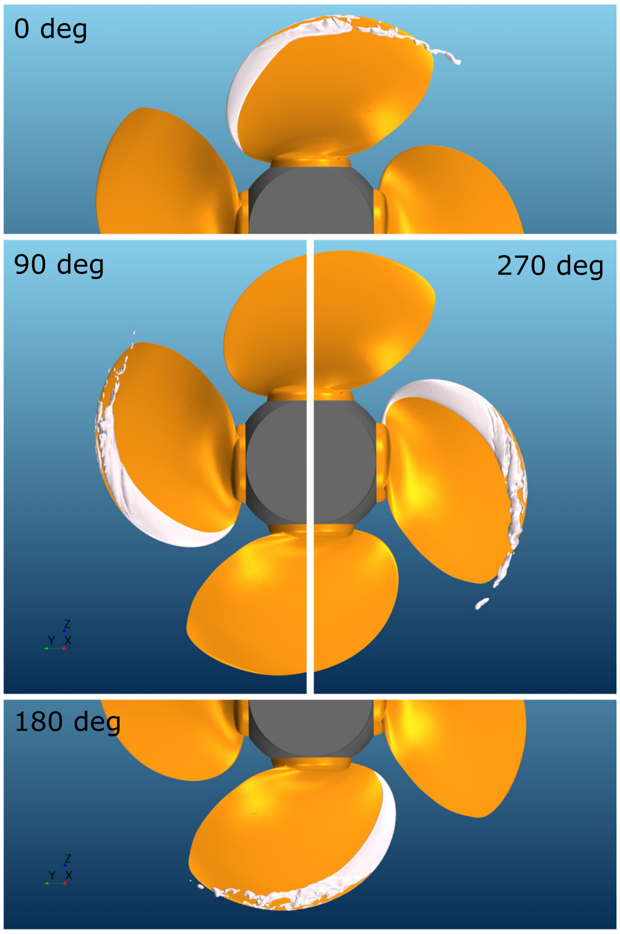

FIG. 16. Instantaneous vapor volume on the refined blade of design 1 at 0, 90, 180, and 270 propeller position.

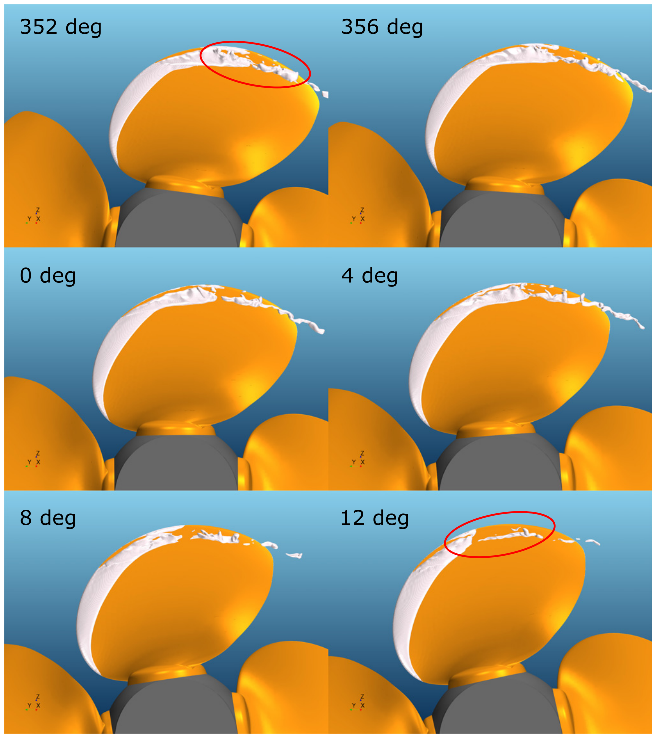

FIG. 17. Instantaneous vapor volume on the refined blade of design 1 around the top position.

focusing. That is a common observation since the instantaneous release of energy usually leads to higher accumulated surface energy. Whether the surface energy will be higher or lower than the one predicted with energy focusing depends strongly on the dynamics and the location of the radiation sources, as well as the curvature of the blade surface. Usually, the shedding of the sheet cavity happens very close to the surface, and the non-focusing model tends to produce larger amounts of energy on the surface. However, it can happen that the radiation sources with energy focusing are much closer to the surface than without focusing. Apparently, that happens to the second design where the surface accumulated energy is very similar for both approaches, and slightly higher in some revolutions, when energy focusing is applied.

Looking at the surface energy distribution on the blade, we can get a better insight into the locations of high implosion loads and the blade areas of higher erosion risk. Figure 22 illustrates the energy distribution on each design, without and with energy focusing. First of all, as in all the previous test cases, the energy focusing approach predicts higher implosion loads on the blades, the impacts on the surfaces are more scattered, and the main impacted areas are more distinct. Additionally, as the energy radiation takes place only at the final stage of the collapse, the involved advection has the tendency to stretch the surface energy distribution further downstream. Much less energy is predicted close to the leading edge, and the energy is concentrated slightly further downstream in chord-wise direction. On the other hand, when no energy focusing is applied, the radiated energy is extended over a larger area, and consequently, lower magnitudes are expected and at locations closer to the leading edge. This observation is less pronounced on design 2, as it shows more similar impact distributions with and without energy focusing. One possible explanation could be that the vapor cavities that are of smaller size do not collapse very far from the point they are shed, and even though the pressure recovery gradient is not as pronounced as in design 1 (see Fig. 13), it is still sufficient to cause rapid collapses, without letting the cavities travel long distances during their collapse. Thus, the effect of the focusing is mainly visible on the magnitude and not the location of the implosions.

On design 1, almost no energy is predicted over the mid-span of the blade with energy focusing. Most of the radiated energy is concentrated at the top of the blade and at higher radii. Much higher amplitudes of the implosion loads are predicted for design 1, showing a higher erosion risk than design 2, which compares well with both the MPUF calculations, and the overall observations on the real blades. Furthermore, design 1 should experience erosion in a wide range of conditions, but it can be expected that at low speed, the erosion risk is very high. On the contrary, design 2 did not show any severe pressure side cavitation at 19 knots based on the full-scale observations, and therefore not a real risk for erosion, but at approximately 13.5 knots,

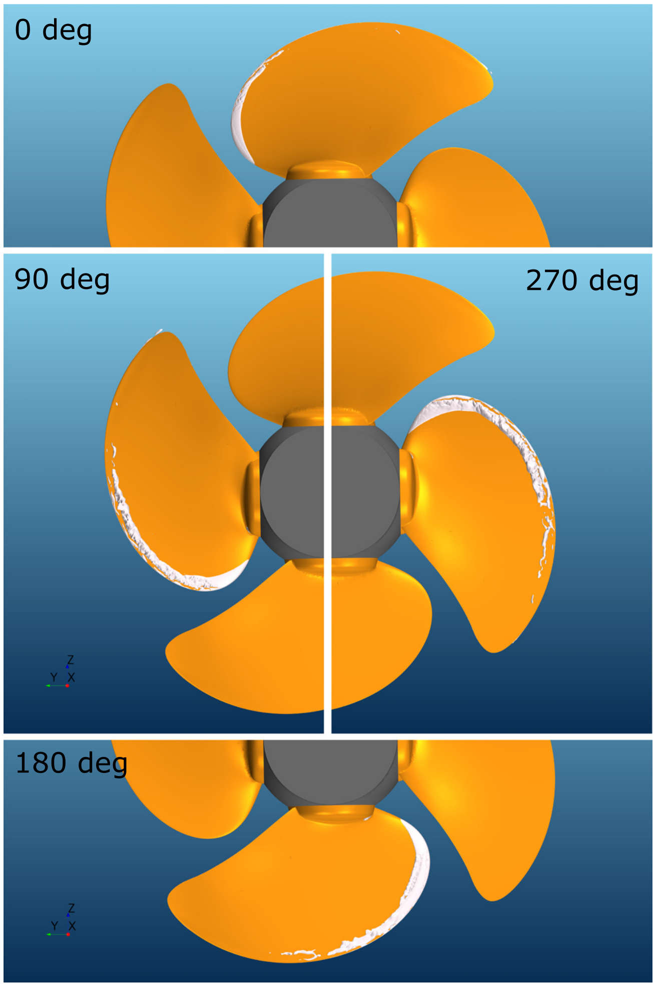

FIG. 18. Instantaneous vapor volume on the refined blade of design 2 at 0, 90, 180, and 270 propeller position.

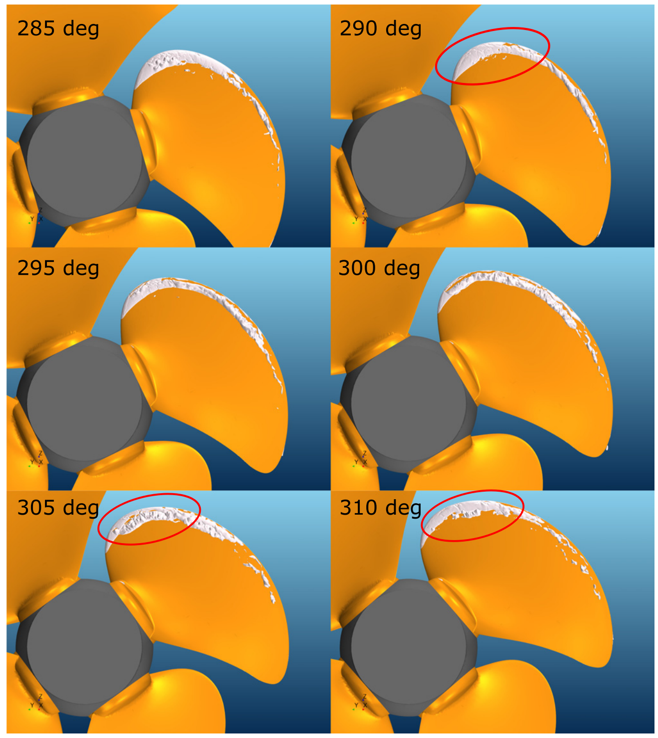

FIG. 19. Instantaneous vapor volume on the refined blade of design 2 showing the high-frequency shedding of the sheet cavity at lower radii.

both observations and simulations show some erosion risk on the blades, however, still lower compared to design 1.

A filter has been applied to attenuate the low-amplitude events, usually of high frequency, so that extreme events can be identified. Cavitation erosion can be a result of both repetitive events of low amplitude, and less frequent extreme events, but in most of the cases, the extreme events are the ones mainly responsible for material damage. Figures 23 and 24 present the filtered averaged surface impact distribution for designs 1 and 2, respectively, and for five variations of the intensity exponent ($n = 1.5$, 2, 3, 4, and 5). The unfiltered distribution ($n = 1$) is the total accumulated energy as shown in Fig. 22. The filtered distribution attenuates the low-amplitude events and amplifies the extreme events. Since the applied filter is derived by normalizing the amplified impact power by its maximum value and has a value between 0 and 1, the filtered energy amplitudes cannot be higher than the unfiltered energy distribution. Therefore, a different colorbar is used for the unfiltered energy distribution for a better comparison.

Looking at the filtered surface energy distribution, already for $n = 1.5$ we observe that the impact scatter has increased compared to the unfiltered distribution ($n = 1$). For large exponents ($n > 2$), the filtered distribution looks very similar, without any significant change in the location of the extreme loads. That could mean that the high loads identified for large exponents are much higher than the loads at other locations of the blade. The distribution obtained for large exponents should give a better indication of the actual damage on the real blade that originated from these extreme events, although larger sample time (and revolutions) is needed for a statistical averaged solution, compared to the unfiltered distribution. Based on both the filtered and the unfiltered energy distribution, design 1 indicates a very high risk for erosion at the identified locations, and from the filtered distribution, it is illustrated that much higher impact loads occur on design 1. The energy distribution on design 2 identifies two main impact locations close to the leading edge, one at about 0.6R–0.75R and one at 0.9 R. From the unfiltered surface energy distribution ($n = 1$), it is not clear which, of the two locations, has a higher erosion risk. On the other hand, the filtered surface energy distribution for high exponents identifies the impact at the lower radii to be of quite higher amplitude and therefore indicating a higher risk of erosion in that region.

The surface specific energy over the percentage of the impacted area confirms the conclusions of the analysis so far (see Fig. 25). The surface specific energy is higher when predicted with the focusing approach, compared to the one without energy focusing, for both designs. As the blade area approaches the minimum cell surface, as

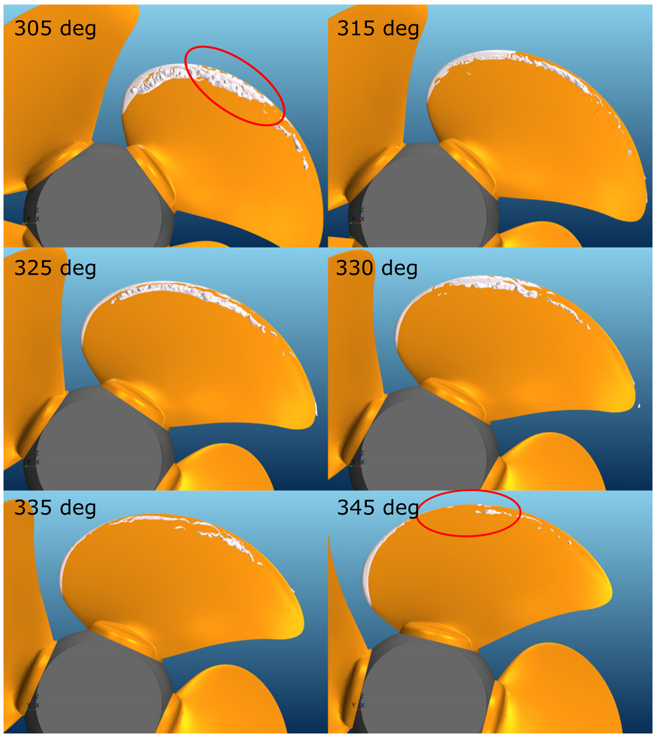

FIG. 20. Instantaneous vapor volume on the refined blade of design 2 showing the cloud cavitation at higher propeller radii, associated with a low-frequency shedding.

defined by the mesh size, a stepped increase in the surface specific energy is observed. This is more pronounced when energy focusing is applied, since the radiated energy is accumulated in smaller volumes, and therefore projected to smaller surface areas. A similar percentage of blade area is impacted on each design (about 10%). However, design 1 exhibits 2–3 times higher implosion loads than design 2. The difference is smaller when no energy focusing is applied, indicating that energy focusing is essential for a fair comparison between the erosion risk of different designs (or even operating conditions). Consequently, the total accumulated surface energy, the blade impact distribution,

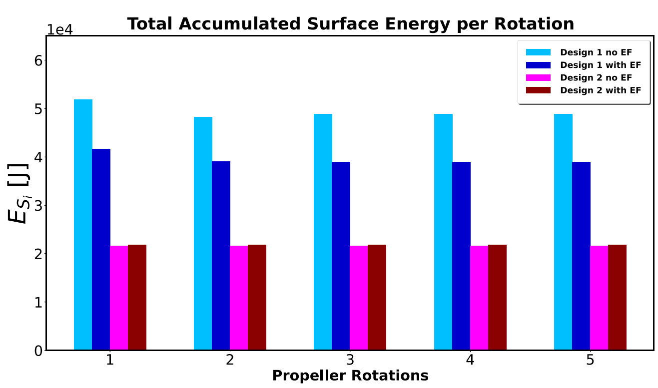

FIG. 21. Total accumulated surface energy per propeller rotation, for five consecutive revolutions, for both designs, with and without energy focusing.

and the surface specific energy plot indicate a higher erosion risk for design 1, and based on the implosion load amplitudes, design 1 should exhibit erosion damage quite quicker than design 2, at the same operating condition.

Finally, we have compared the surface impact distribution obtained from the simulations to the actual damage on the real blades. Figure 26 presents snapshots of the blades of designs 1 and 2, where erosion damage is observed. Unfortunately, only a part of the blades is visible, but possibly only these parts suffered from erosion damage. The CFD solution has been plotted on the real blades for a fair and direct comparison. For a better illustration, only energy amplitudes above 100 and 10 KJ/m^2 are considered for the unfiltered ($n = 1$) and filtered ($n = 5$) surface specific energy distributions, respectively. It is important to note that the time after which the snapshots were taken is not known, and therefore, the intensity of the damage is not representative. Based on the observations and the simulations, for instance, design 1 shows a higher risk, and more damage should be seen on the blades. However, the snapshot of design 2 shows more severe erosion on the blade. Apparently, when the snapshot was taken, design 2 was much longer in operation than design 1. It has also been communicated by the owner that the blades of design 1 were more frequently repaired, and the removed material was replaced by means of welding. Comparing the damage locations, the predicted impact distributions agree very well with some regions of the real damage on the blades. Especially on design 2, where erosion takes place within a much smaller range of operating conditions than design 1, the correlation between predictions and actual damage location is pretty good. Based on the unfiltered surface energy, a second location on the blade showed high accumulated energy, at higher radii and closer to the tip (see Fig. 22). Nevertheless, the filtered energy showed that the implosion events at lower radii are more extreme, and the erosion risk is much higher, agreeing well with the actual erosion on the real blade. The actual damage pattern on design 1 is probably originated from a combination of conditions, since it exhibits pressure side cavitation over a longer range of operating conditions. A large area along the leading edge seems to be impacted from cavitation erosion. Comparing the damage location with the predicted blade impact distribution, it agrees well with one region of the actual damaged area. However, no energy is predicted at lower radii, where material damage is detected on the real blade. Apparently, those locations have been impacted from operating at higher speeds and absorbed power, where a smaller amount of pressure side cavitation is present, and consequently, higher impacts at lower radii are expected.

V. DISCUSSION

Energy focusing appears essential to have a quantitative high-fidelity prediction of the cavitation implosion loads. Neglecting the energy focusing usually leads to larger amounts of total accumulated energy on the blade surface, as well as lower amplitudes in critical areas of the blade. Due to the instantaneous energy radiation during any negative vapor volume change, energy is emitted at an earlier stage, way before the actual location of the final collapse, resulting in a wider and less intense energy distribution. Therefore, it is crucial for both the amplitude and the location of the implosion loads to always account for energy focusing, so that the overall as well as the instantaneous energy balance is always satisfied. This conclusion is in accordance with the results of previous studies.[41,42]

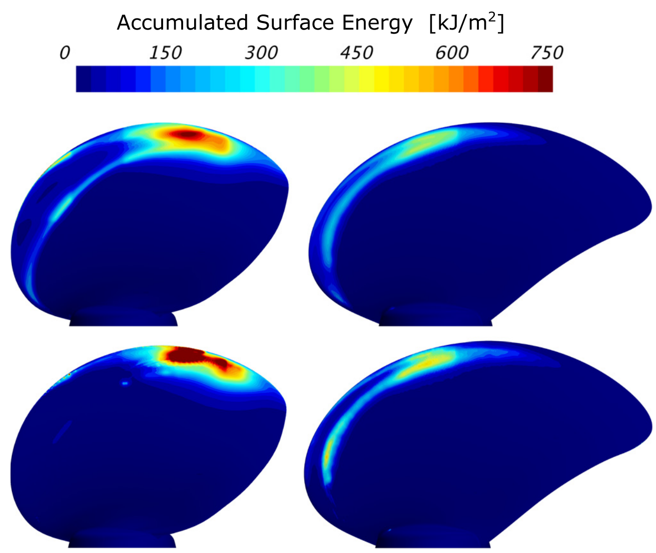

FIG. 22. Surface specific accumulated energy on the refined propeller blade of design 1 (left) and design 2 (right), obtained without (top) and with (bottom) energy focusing, after five propeller revolutions.

The erosion risk on design 1 is clearly higher than the erosion risk on design 2. First, the total accumulated energy on the blade during each propeller revolution is higher than for the second design. Furthermore, the surface impact distribution shows higher accumulated energy amplitudes at a distinct location for design 1, and finally, a closer look at the surface specific energy indicates that design 1 suffers from impact loads with amplitudes of about two times higher than the ones on design 2. Nevertheless, the accumulated surface energy distribution on design 2 is in better agreement with the actual erosion damage location on the real blade, than for design 1. A possible explanation for this discrepancy is that design 1 experiences erosion damage in a wider range of operating conditions than design 2, while we only simulated the implosion loads for one operating condition. The erosion risk at low speed appears to be the highest, considering the larger vapor volume and the larger energy content within the collapsing cavities. This justifies also the fact that the damage location at this condition is predicted further downstream and at higher radii. At higher ship speeds, the amount of pressure side cavitation is considerably less, probably resulting in implosion loads closer to the leading edge and lower radii. Therefore, the actual damage profile on the real blade of design 1 is rather complicated to simulate exactly, as it should come from a combination of several conditions. However, the simulated damage location agrees well with one region of the actual damaged area on the real blade.

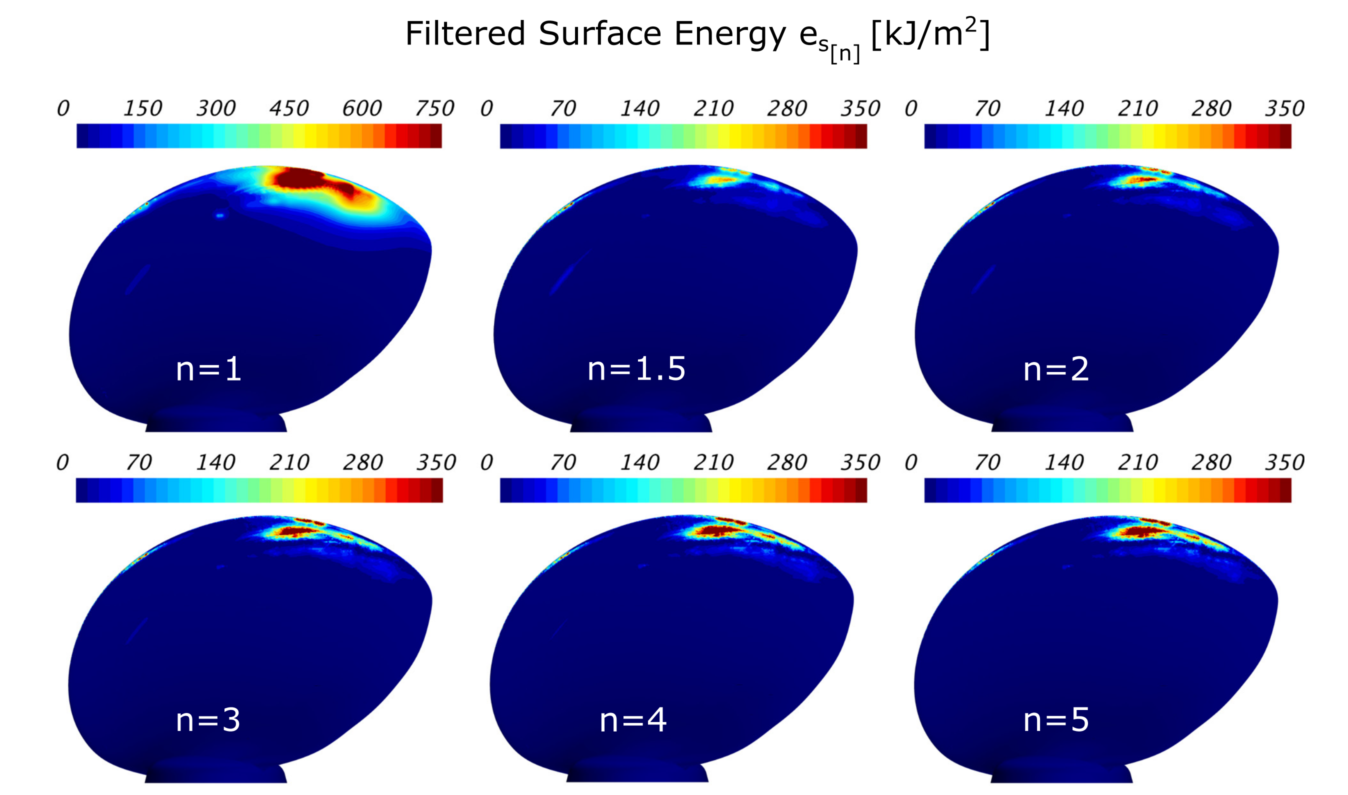

FIG. 23. Filtered averaged surface impact distribution for different intensity exponents n, for design 1, after 5 propeller revolutions.

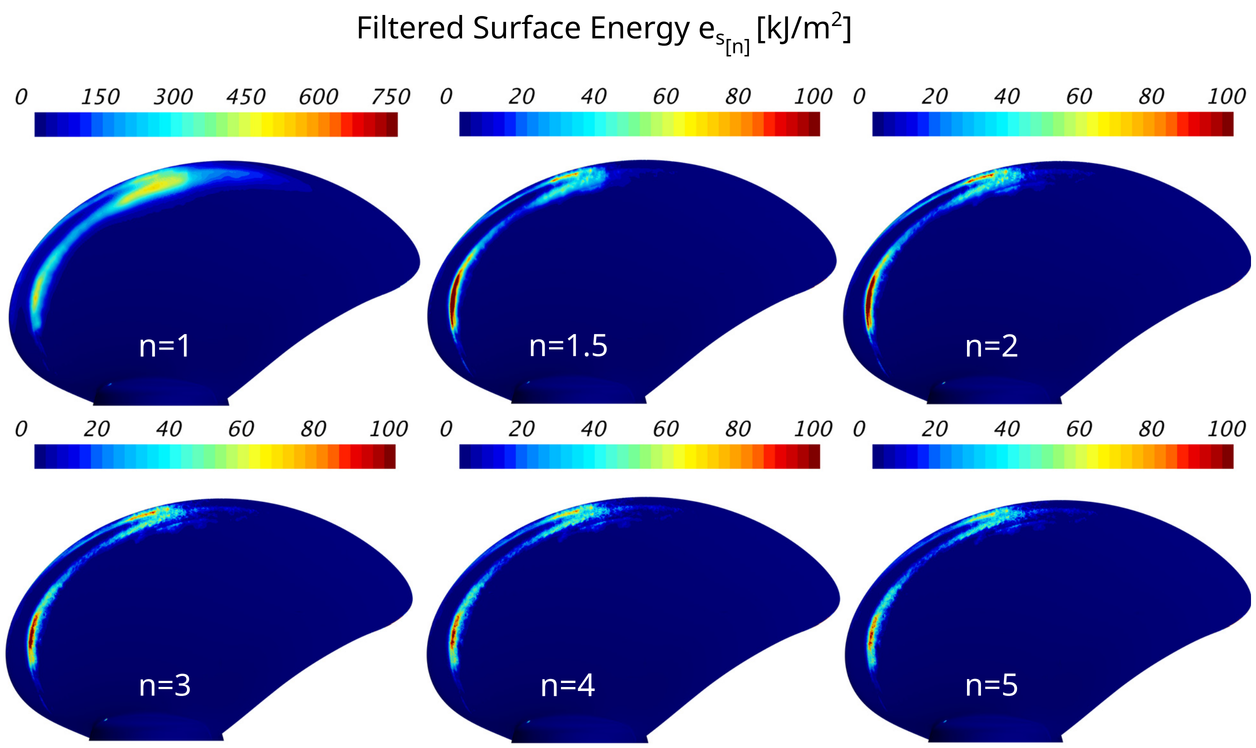

FIG. 24. Filtered averaged surface impact distribution for different intensity exponents n, for design 2, after 5 propeller revolutions.

On the other hand, design 2 showed very little pressure side cavitation at high ship speeds, and based on the observations, only at low speed seemed to suffer from cavitation erosion. This explains why a very good agreement with the damage pattern is obtained, as the simulated operating condition is probably the one responsible for the erosion damage.

It should be noted that there is some uncertainty regarding the actual geometry of both sets of blades. It was reported that the blades of design 1 have been repaired several times. During these repairs, the eroded areas have been ground out, and the areas on the blades where material has been removed have been welded. Due to the erosion and the repairs, the leading edges of the blades have become much thinner and the chord of the blades has also been reduced. The thin and sharp leading edges may increase the amount of cavitation and the severity of its dynamics. It is also not completely clear how often the blades of design 2 have been repaired. It seems, however, that they are closer to their original geometry (used in the simulations) than design 1.

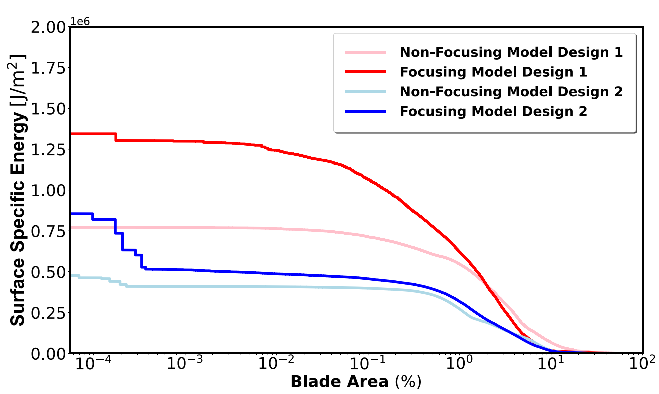

FIG. 25. Surface specific energy over the blade area, showing the extent of the impacted blade area for each design, after five propeller revolutions, with and without energy focusing.

The collapse driving pressure still remains the most difficult quantity to assess in the presented modeling framework and introduces the highest uncertainty. The reason is that the collapsing driving pressure is an unsteady and non-uniform ambient condition. For periodic cavitating flows typically encountered in engineering problems, the proposed moving time-averaged pressure gives a good approximation of the collapsing driving pressure and allows to capture the effect of the pressure recovery gradients on a statistical average. However, a more detailed model with a stronger physical foundation would be desirable for the driving pressure.

Another uncertainty that should be considered is the turbulence model. Propeller flows in behind condition are highly curved and contain swirling vortices, resulting in instabilities and anisotropic behavior. On the other hand, RANS modeling assumes isotropic turbulence and the Reynolds stresses are proportional to the mean strain rate tensor. Therefore, eddy viscosity models may fail to capture cavitation inception and proper cavity shedding, and usually, vortex flows dissipate quickly due to large values of eddy viscosity. Based on previous studies,[48] correcting the eddy viscosity at the liquid–vapor interface leads to better predictions of the shedding of partial cavities and

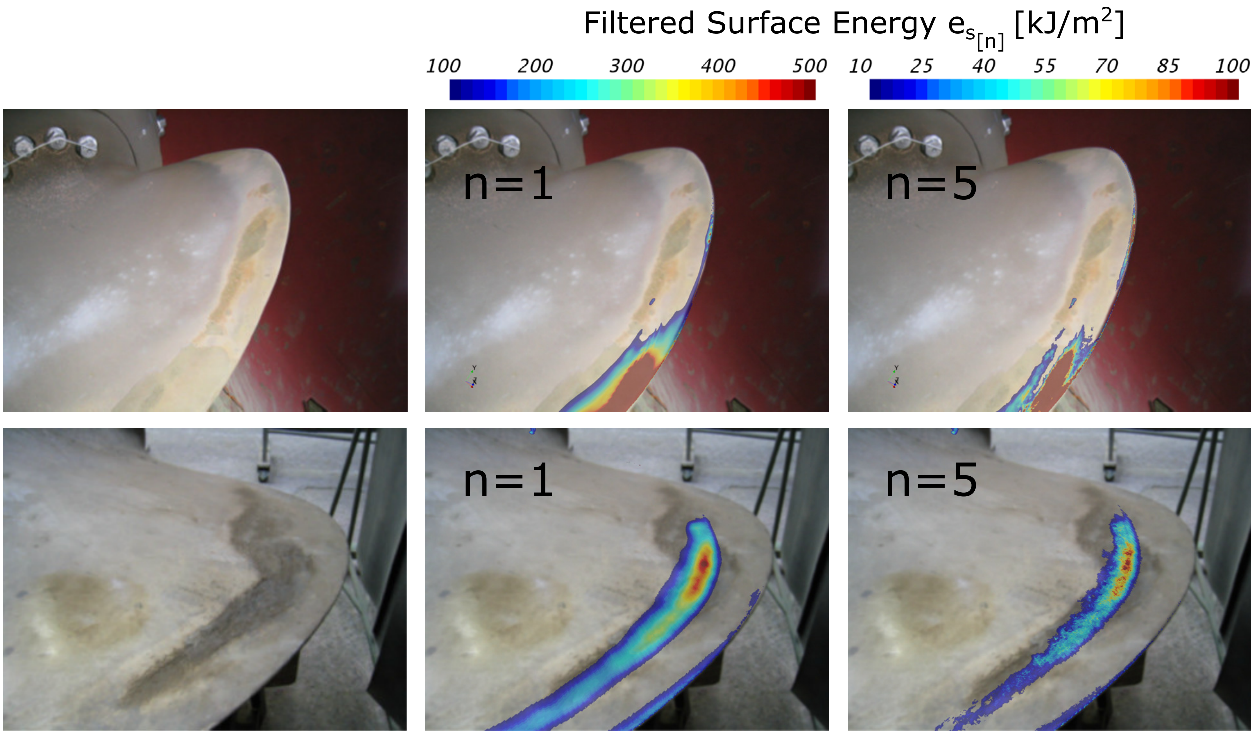

FIG. 26. Comparison between the simulated filtered surface energy and the actual damage on the real blade for design 1 (top) and design 2 (bottom). The filtered surface energy predicted with CFD is plotted on the snapshot of the real blade for two intensity components $n = 1$ (unfiltered distribution and total accumulated surface energy) and $n = 5$.

URANS models are able to predict the larger hydrodynamic scales combined with sufficient resolution in space and time. Thus, in this study, the main focus has been to resolve the larger scales and neglect smaller scales and secondary flows (e.g., small size bubbles, liquid-jet mechanism, and tip vortices). Using more detailed turbulence models (e.g., RSM, DES, and LES) to resolve smaller scale dynamics can lead to more accurate predictions of the vapor volume and therefore to higher fidelity erosion risk assessment.

VI. CONCLUSION

The erosion risk on the propeller blades behind a Ro–Ro container vessel has been assessed for two propeller designs. Larger amounts of pressure side cavitation have been found on the blades of design 1, resulting in higher accumulated energy on the surface. Design 2 showed two characteristic shedding mechanisms during each propeller revolution, resulting, however, in lower implosion loads and lower erosion risk, based on the presented erosion risk analysis.

The erosive aggressiveness of the flow has been investigated by isolating extreme loads on the blade surface. For an intensity exponent $n > 2$, the lower amplitudes are sufficiently attenuated, and the filtered energy distribution does not change for higher exponents. Very large values for the exponent n ($n > 5$) may lead to precision errors due to excessive magnitudes of the amplified radiation terms. It is therefore recommended to always use exponent values between 2 and 5 ($2 < n < 5$) in order to filter low-amplitude events from the surface impact distribution. Two main differences have been observed between the filtered and the unfiltered distribution. First, the filtered impacts are more scattered, since the extreme events are less frequent, but more pronounced. Second, the distribution looks slightly shifted toward the tip for both designs. Extreme events are more likely to occur at locations where the pressure has already recovered, and the driving pressure is the largest. Therefore, by increasing n, the location of the impacts tends to be correlated with locations of high driving pressures.

Two high erosion risk areas were found on the blade surface of design 2. It was not possible to identify which of the two locations has a higher erosion risk from the unfiltered surface energy distribution (accumulated surface energy, $n = 1$). On the other hand, the filtered surface energy distribution for large intensity exponents ($n > 2$) identifies the impact at the lower radii to be of quite higher amplitude, and therefore indicating a higher risk of erosion in that region. This result agrees well with the actual damage on the real blade.

Based on the results from this study, it is hypothesized that the proposed methodology, which accounts for energy focusing during the collapse, is able to give a good indication of the risk and location of cavitation erosion damage. Of course, the damage extent will always be underestimated since, first, not all the flow features are resolved, and second, the simulations are performed for a few seconds, while the real propeller operates for thousands of hours. Finally, the uncertainty of the operational profile and its consequences for risk and location of erosion damage should also be considered.

ACKNOWLEDGMENTS

This research has been funded by the European Union Horizon 2020 Research and Innovation program, Grant Agreement No. 642536, by the Propulsion Technology Department of Wärtsilä Netherlands in Drunen, and by the Maritime and Transport Technology Department at Technical University of Delft. We also highly appreciate Dr. Maarten Bijlard (Wärtsilä Netherlands) for his valuable input and help in the post-processing of the data, and Professor Christian Poelma (TU Delft) for reviewing this work.

AUTHOR DECLARATIONS

Conflict of Interest

The authors have no conflicts to disclose.

Author Contributions

Themistoklis Melissaris: Conceptualization (equal); Investigation (equal); Methodology (equal); Software (equal); Validation (equal); Visualization (equal); Writing – original draft (equal). **Soeren Schenke:** Conceptualization (equal); Methodology (equal); Writing – review & editing (equal). **Tom J. C. van Terwisga:** Conceptualization (equal); Methodology (equal); Supervision (equal); Writing – review & editing (equal).

DATA AVAILABILITY

The data that support the findings of this study are available on request from the corresponding author.

REFERENCES

[1]C. S. Köksal, O. Usta, B. Aktas, M. Atlar, and E. Korkut, "Numerical prediction of cavitation erosion to investigate the effect of wake on marine propellers," Ocean Eng. **239**, 109820 (2021).
[2]L. Rayleigh, "On the pressure development in a liquid during the collapse of a spherical cavity," Philos. Mag. **34**, 94–98 (1917).
[3]M. S. Plesset and A. Prosperetti, "Bubble dynamics and cavitation," Annu. Rev. Fluid Mech. **9**, 145–185 (1977).
[4]J.-C. Isselin, A.-P. Aloncle, and M. Autric, "On laser induced single bubble near a solid boundary: Contribution to the understanding of erosion phenomena," J. Appl. Phys. **84**, 5766 (1998).
[5]A. Philipp and W. Lauterborn, "Cavitation erosion by single laser-produced bubbles," J. Fluid Mech. **361**, 75–116 (1998).
[6]R. T. Knapp, "Recent investigations of the mechanics of cavitation and cavitation damage," Trans. ASME **1045**, 1045–1054 (1955).
[7]M. J. Robinson and F. G. Hammitt, "Detailed damage characteristics in cavitation venturi," Trans. ASME, J. Basic Eng. **89**, 161–173 (1967).
[8]T. Okada, Y. Iwai, and K. Awazu, Wear **133**, 219–232 (1989).
[9]T. Momma and A. Lichtarowicz, "A study of pressures and erosion produced by collapsing cavitation," Wear **186–187**, 425–436 (1995).
[10]M. S. Plesset and R. B. Chapman, "Collapse of an initially spherical vapour cavity in the neighbourhood of a solid boundary," J. Fluid Mech. **47**, 283–290 (1970).
[11]M. Dular, B. Stoffel, and B. Sirok, "Development of a cavitation erosion model," Wear **261**, 642–655 (2006).
[12]R. Fortes-Patella and J. L. Reboud, "A new approach to evaluate the cavitation erosion power," J. Fluids Eng. **120**, 335–344 (1998).
[13]S. Joshi, J. P. Franc, G. Ghigliotti, and M. Fivel, "Sph modelling of a cavitation bubble collapse near an elasto-visco-plastic material," J. Mech. Phys. Solids **125**, 420–439 (2018).
[14]G. Bark, N. Berchiche, and M. Grekula, *Application of Principles for Observation and Analysis of Eroding Cavitation, EROCAV Observation Handbook*, 3rd ed. (Chalmers University of Technology, Sweden, 2004).
[15]M. Grekula and G. Bark, "Analysis of high-speed video data for assessment of the risk of cavitation erosion," in *Proceedings 1st International Conf. on Advanced Model Measurement Technology for EU Maritime Industry (AMT09)* (Ecole Centrale de Nantes, Nantes, France, 2009), pp. 83–100.
[16]G. Bark and R. Bensow, "Hydrodynamic mechanisms controlling cavitation erosion," Int. Shipbuilding Prog. **60**, 345–374 (2013).
[17]W. Pfitsch, S. Gowing, and D. Fry, "Development of measurement techniques for studying propeller erosion damage in severe wake fields," in Proceedings of the 7th International Symposium on Cavitation Ann Arbor, MI, 2009.
[18]J.-K. Choi and G. L. Chahine, "Experimental and numerical study of cavitation erosion resistance of a polyurea coating layer," in Proceedings of the 4th Symposium on Marine Propulsors (SMP15) Austin, TX, 2015.
[19]Y. Cao, X. X. Peng, and K. A. Yan, "A qualitative study on the relationship between cavitation structure and erosion region around a 3D twisted hydrofoil by painting method," in Proceedings of the 5th Symposium on Marine Propulsors (SMP17), Helsinki, Finland, 2017.
[20]G. Bark, J. Friesch, G. Kuiper, and J. Ligtelijn, "Cavitation erosion on ship propellers and rudders," in Proceedings of the 9th Symposium on Practical Design of Ships and Other Floating Structures, Luebeck-Travenmuende, Germany, 2004.
[21]N. Hasuike, S. Yamasaki, and J. Ando, "Numerical study on cavitation erosion risk of marine propellers operating in wake flow," in Proceedings of the 7th International Symposium on Cavitation, Ann Arbor, MI, 2009.
[22]N. Nohmi, Y. Iga, and T. Ikohagi, "Numerical prediction method of cavitation erosion," in Proceedings of the FEDSM, Jacksonville, 2008.
[23]N. X. Lu, R. Bensow, and G. Bark, "Large eddy simulation of cavitation development on highly skewed propellers," J. Mar. Sci. Technol. **19**, 197–214 (2013).
[24]O. Usta, B. Aktas, M. Maasch, O. Turan, M. Atlar, and E. Korkut, "A study on the numerical prediction of cavitation erosion for propellers," in Proceedings of the 5th International Symposium on Marine Propulsors, Espoo, Finland, 2017.
[25]O. Usta and E. Korkut, "Prediction of cavitation development and cavitation erosion on hydrofoils and propellers by detached eddy simulation," Ocean Eng. **191**, 106512 (2019).
[26]A. Peters, U. Lantermann, and O. el Moctar, "Numerical prediction of cavitation erosion on a ship propeller in model- and full-scale," Wear **408–409**, 1–12 (2018).
[27]M. H. Arabnejad, A. Amini, M. Farhat, and R. Bensow, "Hydrodynamic mechanism of aggressive collapse events in leading edge cavitation," J. Hydrodyn. **32**, 6–19 (2020).
[28]M. H. Arabnejad, U. Svennberg, and R. E. Bensow, "Numerical assessment of cavitation erosion risk using incompressible simulation of cavitating flows," Wear **464**, 203529 (2021).
[29]M. S. Mihatsch, S. J. Schmidt, M. Thalhamer, and N. A. Adams, "Numerical prediction of erosive collapse events in unsteady compressible cavitating flows," in Proceedings of IV International Conference on Computational Methods in Marine Engineering, Lisbon, Portugal, 2011.
[30]S. Mottyll and R. Skoda, "Numerical 3D flow simulation of ultrasonic horns with attached cavitation structures and assessment of flow aggressiveness and cavitation erosion," Ultrason. Sonochem. **31**, 570–589 (2016).
[31]B. Budich, S. J. Schmidt, and N. Adams, "Numerical simulation and analysis of condensation shocks in cavitating flow," J. Fluid Mech. **838**, 759–813 (2018).
[32]N. Ochiai, Y. Iga, and M. Nohmi, "Study of quantitative numerical prediction of cavitation erosion in cavitating flow," J. Fluids Eng. **135**, 011302 (2013).
[33]D. Ponkratov and A. Caldas, "Prediction of cavitation erosion by detached eddy simulation (DES) and its validation against model and ship scale results," in Proceedings of the 4th International Symposium on Marine Propulsors, Austin, TX, 2015.
[34]D. Ponkratov, "DES prediction of cavitation erosion and its validation for a ship scale propeller," J. Phys. Conf. Ser. **656**, 012055 (2015).
[35]F. G. Hammit, "Observations on cavitation damage in a flowing system," J. Basic Eng. **85**, 347–356 (1963).
[36]A. Vogel and W. Laterborn, "Acoustic transient generation by laser-produced cavitation bubbles near solid boundaries," J. Acoust. Soc. Am. **84**, 719–731 (1988).
[37]C. Flageul, R. Fortes-Patella, and A. Archer, "Cavitation erosion prediction by numerical simulations," in Proceedings of the 14th International Symposium on Transport Phenomena and Dynamics of Rotating Machinery, Honolulu, HI, 2012.

[38]C. Leclercq, A. Archer, R. Fortes-Patella, and F. R. F. Cerru, "Numerical cavitation intensity on a hydrofoil for 3D homogeneous unsteady viscous flows," Int. J. Fluid Mach. Syst. **10**, 254–263 (2017).
[39]R. Fortes-Patella, G. Challier, J. L. Reboud, and A. Archer, "Energy balance in cavitation erosion: From bubble collapse to indentation of material surface," J. Fluids Eng. **135**, 011303 (2013).
[40]S. Schenke, "Cavitation implosion loads from energy balance considerations in numerical flow simulations," Ph.D. thesis (Delft University of Technology, Delft, The Netherlands, 2020).
[41]T. Melissaris, S. Schenke, N. Bulten, and T. J. C. van Terwisga, "On the accuracy of predicting cavitation impact loads on marine propellers," Wear **456–457**, 203393 (2020).
[42]T. Melissaris, S. Schenke, N. Bulten, and T. J. C. van Terwisga, "Cavitation erosion risk assessment on a full-scale steerable thruster," Ocean Eng. **251**, 11019 (2022).
[43]S. Muzaferija, M. Peric, P. Sames, and T. Schelin, "A two-fluid Navier-Stokes solver to simulate water entry," in Twenty-Second Symposium on Naval Hydrodynamics, Washington, DC, 1998.
[44]B. P. Leonard, "The ultimate conservative difference scheme applied to unsteady one-dimensional advection," Comput. Methods Appl. Mech. Eng. **88**, 17–74 (1991).
[45]T. Waclawczyk and T. Koronowicz, "Modeling of the wave breaking with CICSAM and HRIC high-resolution schemes," in European Conference on Computational Fluid Dynamics (ECCOMAS CFD 2006), Delft, The Netherlands (2006).
[46]F. Menter, "Two-equation eddy-viscosity turbulence modeling for engineering applications," AIAA J. **32**, 1598–1605 (1994).
[47]J.-L. Reboud and Y. Delannoy, "Two-phase flow modelling of unsteady cavitation," in Proceedings of the 2nd International Symposium on Cavitation, Tokyo, Japan, 1994.
[48]T. Melissaris, N. Bulten, and T. J. C. van Terwisga, "On the applicability of cavitation erosion risk models with a URANS solver," J. Fluids Eng. **141**, 101104 (2019).
[49]G. H. Schnerr and J. Sauer, "Physical and numerical modeling of unsteady cavitation dynamics," in Fourth International Conference on Multiphase Flow, New Orleans, 2001.
[50]T. Huuva, "Large eddy simulation of cavitating and non-cavitating flow," Ph.D. thesis (Chalmers University of Technology, Sweden, 2008).
[51]L. Eca, F. S. Pereira, and G. Vaz, "Viscous flow simulations at high Reynolds numbers without wall functions: Is $y^+ \simeq 1$ enough for the near-wall cells?," Comput. Fluids **170**, 157–175 (2018).
[52]M. Tinguely, D. Obreschkow, P. Kobel, N. Dorsaz, A. de Bosset, and M. Farhat, "Energy partition at the collapse of spherical cavitation bubbles," Phys. Rev. E **86**, 046315 (2013).
[53]B. P. Welford, "Note on a method for calculating corrected sums of squares and products," Technometrics **4**, 419–420 (1962).
[54]S. Schenke, T. Melissaris, and T. J. C. van Terwisga, "On the relevance of kinematics for cavitation implosion loads," Phys. Fluids **31**, 052102 (2019).